

Flexible Humidity Sensors Based on Aerosol Printed Green Graphene Inks

by

Mohsen KETABI

THESIS PRESENTED TO ÉCOLE DE TECHNOLOGIE SUPÉRIEURE
IN PARTIAL FULFILLMENT FOR A DEGREE OF MASTER'S
WITH THESIS IN ELECTRICAL ENGINEERING
M. Sc. A.

MONTREAL, MARCH 23, 2022

ÉCOLE DE TECHNOLOGIE SUPÉRIEURE
UNIVERSITÉ DU QUÉBEC



Mohsen Ketabi, 2022



This Creative Commons licence allows readers to download this work and share it with others as long as the author is credited. The content of this work can't be modified in any way or used commercially.

BOARD OF EXAMINERS
THIS THESIS HAS BEEN EVALUATED
BY THE FOLLOWING BOARD OF EXAMINERS

Mr. Ricardo Izquierdo, Thesis Supervisor
Department of Electrical Engineering, École de technologie supérieure

Mr. Sylvain Cloutier, President of the Board of Examiners
Department of Electrical Engineering, École de technologie supérieure

Mr. Frederic Nabki, Member of the jury
Department of Electrical Engineering, École de technologie supérieure

THIS THESIS WAS PRESENTED AND DEFENDED
IN THE PRESENCE OF A BOARD OF EXAMINERS AND PUBLIC
MARCH 7, 2022
AT ÉCOLE DE TECHNOLOGIE SUPÉRIEURE

ACKNOWLEDGMENT

Numerous people contributed to my success with this essay. I would like to express my sincere gratitude to my advisor, Professor Ricardo Izquierdo at École de Technologie Supérieure, whose honesty and motivation I will never forget. I am grateful for his constant support, guidance, and assistance. He not only allowed me to work in this fascinating area of research, but he also believed in my research and its outcomes. Grateful appreciation to my committee members, Prof. Sylvain Cloutier and Prof. Frederic Nabki, your words of encouragement and detailed feedback have meant a lot to me.

This thesis would not have been possible without the kind support of Dr. Ahmad Al Shboul, whose oversight from the beginning of this study helped to enhance my knowledge of the subject. I am grateful for the extraordinary experiences he arranged for me, as well as the prospects he provided for me to advance professionally. Your name, as well as mine, should appear on this thesis. I would like to extend special thanks to the technical staff at École de Technologie Supérieure and Université du Québec à Montréal, especially Dr. Gwenaël Chamoulaud, Dr. Galyna Shul and Mr. Normand Gravel. I'd want to express my gratitude to all of my research team colleagues.

Nahid, my adoring spouse, I do not know if my words are enough to compensate for your support, patience, and kindness. You were not only a caring mother on this challenging path, but also a solid and tireless companion. I will never forget your everlasting attention. Liana, my beloved daughter, you have been and will remain to be the best and loveliest event in my life. I will never forget what you used to ask me every day “Is your study finished, Let’s play dolls.”

Finally, I am grateful to my wonderful parents for their unwavering love and support, which keeps me motivated and confident. My accomplishments and success are a result of their faith in me. My heartfelt gratitude to my brothers and their families, who showed me how to practice open-hearted positivity, and engage with the world in mindful ethical action.

Capteurs d'humidité flexibles à base d'encre de graphène vert imprimées en Aérosol

Mohsen KETABI

RÉSUMÉ

Dans cette étude, des capteurs d'humidité entièrement flexibles à base de graphène ont été développés et étudiés. Premièrement, trois encres vertes au graphène ont été formulées par l'exfoliation en phase liquide (LPE) de graphite dans des stabilisants biocompatibles (biopolymères) liés à l'eau ; triton X-100, tween-20 et gélatine. Ces produits sont écoresponsables, car ils sont exemptés de les composés organiques volatils (COVs) et de composés nocifs. Les encres au graphène (GGe, GTr et GTw) ont été préparées avec des concentrations optimisées de biopolymères de 0,1 mg.mL⁻¹ de gélatine, 1 mg.mL⁻¹ de triton X-100 et 1,5 mg.mL⁻¹ de tween-20, respectivement. Les films de graphène imprimés par aérosol avec une épaisseur de 500 nm ont montré une résistance de couche (Rs) de 2,6 kΩ/□ pour GTr, 5 kΩ/□ pour GTw et 14 kΩ/□ pour GGe. La faible Rs pour GTr est attribuée à de meilleures propriétés mouillabilité et d'adhérence de l'encre sur les substrats en polyéthylène téréphtalate (PET). Par conséquent, il a été choisi pour développer les capteurs d'humidité en graphène vert.

L'encre GTr a ensuite été modifiée avec diverses concentrations de gélatine pour améliorer la résistance mécanique et les performances de détection d'humidité du capteur. La concentration retenue est de 1 mg/mL et celle-ci est utilisée pour le reste de la recherche. Cette encre (1Ge-GTr) a été imprimée sur des électrodes de carbone sérigraphiées sur un substrat PET, ce qui a donné un capteur d'humidité en graphène vert et flexible. Le 1Ge-GTr a montré une réponse linéaire dans la plage d'humidité relative (HR) de 30 % HR à 90 % HR, une bonne sensibilité de 0,55 %/HR% à 25 °C, une réponse ultrarapide en quelques secondes et une indépendance par rapport aux variations de température allant de 22°C à 70°C. De plus, le capteur a montré une efficacité élevée pour la détection de l'humidité, faisant du capteur un candidat potentiel pour la mise en œuvre dans des applications Internet des objets (IoT) réelles.

Mots-clés: Humidité; capteur; graphène; encre; imprimante aérosol; gélatine; triton X-100; tween-20 ; électronique imprimée.

Flexible humidity sensors based on Aerosol printed green graphene inks

Mohsen KETABI

ABSTRACT

In this study, fully flexible graphene-based humidity sensors were developed and investigated. First, three green graphene inks were formulated by direct liquid exfoliation (LPE) of graphite in water bonded biocompatible stabilizers (biopolymer); triton X-100, tween-20, and gelatin. Ultimately, green and eco-friendly graphene inks were formulated, which are clean of Volatile Organic Compounds (VOCs) and harmful compounds. The graphene inks (namely as GGe, GTr, and GTw) were prepared with optimized biopolymer concentrations of 0.1 mg.mL⁻¹ of gelatin, 1 mg.mL⁻¹ triton X-100, and 1.5 mg.mL⁻¹ tween-20, respectively. The aerosol printed graphene films with 500 nm thickness revealed a sheet resistance (Rs) of 2.6 kΩ/□ for GTr, 5 kΩ/□ for GTw, and 14 kΩ/□ for GGe. The low Rs for GTr was assigned to better ink wettability and adhesion properties on top polyethylene terephthalate (PET) substrates. Therefore, it was chosen for the rest of the research to develop green graphene humidity sensors.

The GTr ink was later modified with various concentrations of gelatin to improve the sensor's mechanical strength and sensing performance for humidity detection. The final product, 1 mg.mL⁻¹ gelatin-modified GTr ink (1Ge-GTr), was selected for the rest of the research. The 1Ge-GTr ink was printed on top of screen-printed carbon electrodes on PET substrate, resulting in a green and flexible graphene humidity sensor. The 1Ge-GTr showed a decent linear response in the relative humidity (RH) range of 30% RH–90% RH, good sensitivity of 0.55%/RH% at 25°C, ultrafast response time in a second, and good independence from temperature fluctuations ranging from 22°C to 70°C. Moreover, the sensor showed a high practical efficiency toward humidity detection, making the sensor a potential candidate for implementation in real-life Internet of Things (IoT) applications.

Keywords: Humidity; sensor; graphene; ink; aerosol printer; gelatin; triton X-100; tween-20; printed electronics.

TABLE OF CONTENTS

INTRODUCTION	25
CHAPITRE 1 LITERATURE REVIEW	27
1.1 Sensors	27
1.1.1 History of Sensors	27
1.1.2 Sensor	29
1.1.3 Classification of Sensors	30
1.1.4 Type of Sensors	30
1.1.5 Humidity Sensor	31
1.1.6 Classification of Humidity Sensors	31
1.2 Printed Electronics	34
1.2.1 Review	34
1.2.2 Aerosol-Jet Printer (AJP)	36
1.3 Graphene and Sensors	36
1.3.1 Resistive Sensors Based on Graphene	38
1.3.2 Graphene Inks	41
CHAPITRE 2 METHODOLOGY	45
2.1 Materials	45
2.2 Preparation of Green Graphene Inks (GGe, GTr, GTw)	45
2.3 Preparation of Gelatin-modified GTr Ink (Ge-GTr)	47
2.4 Sensor Fabrication	47
2.5 Preparation of Screen-printed C-electrodes	51
2.6 Data Collection	51
2.7 Characterization	53
2.7.1 Ultraviolet-visible Spectroscopy (UV-Vis)	53
2.7.2 The Dynamic Light Scattering (DLS)	53
2.7.3 Raman Spectroscopy	54
2.7.4 Atomic Force Microscopy (AFM)	54
2.7.5 Transmission Electron Microscopy (TEM)	55
2.7.6 Scanning Electron Microscope (SEM)	55
2.7.7 Zeta-Potential	56
2.7.8 Thermogravimetric Analysis (TGA)	56
2.7.9 Surface Tension	56
2.7.10 Viscosity	57
2.7.11 Contact Angle	57
2.7.12 4-Probe resistance measurement and Profilometry	57
2.8 Conclusion	58
CHAPITRE 3 GREEN GRAPHENE INKS	59
3.1.1 Biocompatible dispersants	59

3.1.2	Dispersant's ratio	60
3.1.3	Zeta Potentials.....	61
3.1.4	DLS and TGA.....	62
3.1.5	DLS.....	62
3.1.6	TGA	64
3.1.7	AFM and TEM.....	66
3.1.8	Electrical Properties.....	68
3.1.9	4-Probe measurements and Profilometry.....	68
3.1.10	Raman	70
3.1.11	Inks' Wettability and Flake's Interconnectivity: Contact Angle and SEM	71
3.2	Graphene Humidity Sensors	74
3.2.1	GTr Response.....	74
3.2.2	Ge-GTr Response.....	75
3.2.3	Response and Recovery Time.....	77
3.2.4	Temperature Effect	78
3.3	Discussion.....	79
	CONCLUSION.....	81
	FUTURE WORK.....	83
	LIST OF BIBLIOGRAPHICAL REFERENCES.....	85

LIST OF TABLES

		Page
Table 1.1	Comparison between the printing technologies	35
Table 1.2	Comparison of graphene-based chemiresistive humidity sensors	39
Table 1.3	Selected examples of the graphene-based inks and their printable applications	43
Table 3.1	Graphene Flake size distribution as a function of the dispersant and purification process.	64

LIST OF FIGURES

		Page
Figure 0.1	The timeline of the Industrial Revolution	25
Figure 0.2	Overview of IoT Architecture	26
Figure 1.1	The Davy and Geordie lamps are safety lamps for use in flammable atmospheres like coal mines, invented in 1815 by Sir Humphrey Davy and George Stephenson	27
Figure 1.2	The discovery and development of various sensors over time are depicted in this timeline to materials (green), sensor technologies (blue), and biotechnology (black)	28
Figure 1.3	Sensor - Printed and Flexible Sensors 2017-2027_ Technologies, Players, Forecasts_ IDTechEx	29
Figure 1.4	Humidity sensors classification based on the design and used techniques	32
Figure 1.5	Capacitive and resistive humidity sensors	33
Figure 1.6	The different processes of Graphene synthesis	37
Figure 1.7	Graphene-based resistive humidity sensor	38
Figure 2.1	The preparation procedure for the green graphene inks; GTr, GTw, and GGe	46
Figure 2.2	X-Position and Angle Position, Atomizer water level, Aerosol-Jet Printer, Nozzle distance and Atomizer chamber and ink Tube	48
Figure 2.3	Printed GTr films with different printing passes on top PET substrate	48
Figure 2.4	Printed GTr sensor on top screen-printed carbon electrodes pre-prepared on top PET substrate	49
Figure 2.5	Mesh, Zigzag and Ladder Patterns	49
Figure 2.6	Sensing layer on Ag electrode	50
Figure 2.7	Cu, Ag and C electrodes	50
Figure 2.8	(A) Electrodes design by AutoCAD software, (B) Design used to create the mask for screen-printing, (C) Screen-printed electrodes	51

Figure 2.9	(A) Arduino device, (B) Series of sensors in ETS environmental chamber.....	52
Figure 2.10	Sensors printed on carbon electrodes were taken to be tested with humidity at ETS by using the environmental chambers	52
Figure 3.1	Graphene concentration as a function of dispersants' concentration.....	61
Figure 3.2	DLS analysis of the diameter distribution for graphene dispersion prepared with gelatin, triton, and tween dispersants.....	63
Figure 3.3	Thermograms of TGA and derivative (DTG) of raw Gt, gelatin, GGe, GTr and GTw as a function of the dispersant and purification process. (A,B) the gelatin and graphene samples after the centrifugation at 1k rpm for 30 minutes. (C,D) Raw graphite and graphene inks after centrifugation at 14k rpm for 2 hours.....	65
Figure 3.4	AFM images and surface profile from graphene nanosheets from (A) GTr, (B) GTw, and (C,D) GGe. The surface profiles highlight the variation in thickness related to the coating of the adsorbed stabilizers-like residue on the graphene surface	67
Figure 3.5	TEM images of graphene sheets from (A) GTr, (B) GTw, and (C) GGe inks.....	68
Figure 3.6	(A) Optical microscope of Aerosol-Jet printed GTr films on a PET substrate. (B,C) Optical microscope images for a graphene film's edge and center. (D) R_s and (E) σ as a function of films' thickness	70
Figure 3.7	Raman spectra for printed films of the graphene bio-inks.....	71
Figure 3.8	Contact angle measurements for GGe, GTr and GTw over PET substrates.....	72
Figure 3.9	SEM images of graphene films printed from (A,B) GGe, (C,D) GTr, and (E,F) GTw	73
Figure 3.10	The adsorption and desorption response curves for GTr sensor.....	75
Figure 3.11	Optical microscope images of 1Ge-GTr sensors showing the flexible carbon electrodes and the printed graphene thin films	76
Figure 3.12	(A) The adsorption and desorption response curves for Ge-modified GTr sensors. (B) The Summary for adsorption and desorption responses versus humidity for the 1Ge-GTr on the surfaces	76

Figure 3.13	(A) Response and (B) recovery time curve of 1 Ge-GTr based sensor to humidity at working temperature of 25°C.....	78
Figure 3.14	The response curve to temperature for the 1Ge-GTr sensor.....	79

LIST OF ABBREVIATIONS

AB	Absolute Humidity
AFM	Atomic Force Microscopy
Ag	Silver
AJP	Aerosol-Jet Printer
Al	Aluminum
Au	Gold
bp	Boiling point
C	Carbon
CMC	Carboxymethyl cellulose
CMs	Carbon materials
CNT	Carbon nanotube
CRM	Confocal Raman microscope
Cu	Copper
DI	Deionized
DLS	Dynamic light scattering
DMF	Dimethylformamide
DTG	Derivative Thermograms
DUT	Device Under Test
EC	Ethyl Cellulose
EG	Ethylene Glycol
EHD	Electrohydrodynamic

XX

ETS	École de Technologie Supérieure
FETs	Field-Effect Transistors
FG	Fluorinated Graphene
FLEPS	Flexible and Printable Sensors and Systems
FTO	Fluorine-doped Tin Oxide
GA	Gallium
GGe	Graphene gelatin
GO	Graphene oxide
GQDs	Graphene Quantum Dots
GTr	Graphene-triton
GTw	Graphene tween
HSPs	Hansen solubility parameters
HVAC	Heating, ventilation, and air conditioning
IDE	InterDigitated Electrodes
IDT	Interdigital Transducer
IoT	Internet of Things
IPA	Isopropyl alcohol
ITO	Indium Tin Oxide
LPE	Liquid phase exfoliation
MEPAB	2-(Methacryloyloxy)ethyl] Dimethyl Propyl Ammonium Bromide
MMA	Methyl Methacrylate
MPa	Megapascal Pressure

mPa·s	Millipascal-Second
MSCs	Micro-Supercapacitors
MWCNTs	Multi Wall Carbon Nano Tubes
Ni	Nikel
NMP	N-methyl pyrrolidinone
PANI	Polyaniline
PE	Printed Electronics
PEDOT: PSS	Poly(3,4-ethylenedioxythiophene) Polystyrene Sulfonate
PET	Polyethylene terephthalate
PFA	Pore-Forming Agents
PI	Polyimide
PS1	Presenilin-1
Pt	Platinum
PVP	Polyvinylpyrrolidone
rGO	Reduced Graphene Oxide
RH	Relative Humidity
Rs	Sheet resistance
SAW	Surface acoustic waves
SDS	Sodium Dodecyl Sulfate
SEM	Scanning Electron Microscopy
Sn	Tin
TEM	Transmission Electron Microscopy

XXII

TGA	Thermogravimetric analysis
THF	Tetrahydrofuran
Ti	Titanium
UQAM	Université du Québec à Montréal
UV-Vis	Ultraviolet-visible
VOC	Volatile Organic Compounds
XPS	X-ray photoelectron spectroscopy
XRD	X-ray powder diffraction
Zn	Zinc

LIST OF SYMBOLS

Symbol	Measurement	Unit
Ω	Resistance	ohm
Ω/\square	sheet resistivity	ohms/square
μ	Micron	
pL	Picolitre	l
C	Capacitance	F
λ	Wavelength	nm
cP	viscosity	$\text{m}^2 \text{s}^{-1}$
A	Surface	m^2
A	Absorbance	
T	Transmittance	
ϵ	Absorption Coefficient	$\text{cm}^{-1}, /\text{m}^{-1}$
c	Speed of the light	$\text{m}.\text{s}^{-1}$
l	length	m
σ	Conductivity	$\text{uS}.\text{cm}^{-1}, \text{mS}.\text{cm}^{-1}$
t	Thickness	mm
δ_D	Hansen dispersion parameter	$\text{MPa}^{1/2}$
δ_P	Hansen polar parameter	$\text{MPa}^{1/2}$
δ_H	Hansen hydrogen parameter	$\text{MPa}^{1/2}$

INTRODUCTION

The timeline of the Industrial Revolution outlines the major inventions that made a paradigm shift in human lives, beginning with the creation of machines throughout technological and digital revolutions to the fourth industrial revolution; the Smart Factory (or as called the Internet of Things (IoT)), where machines are all interconnected and automated (Figure 0.1).

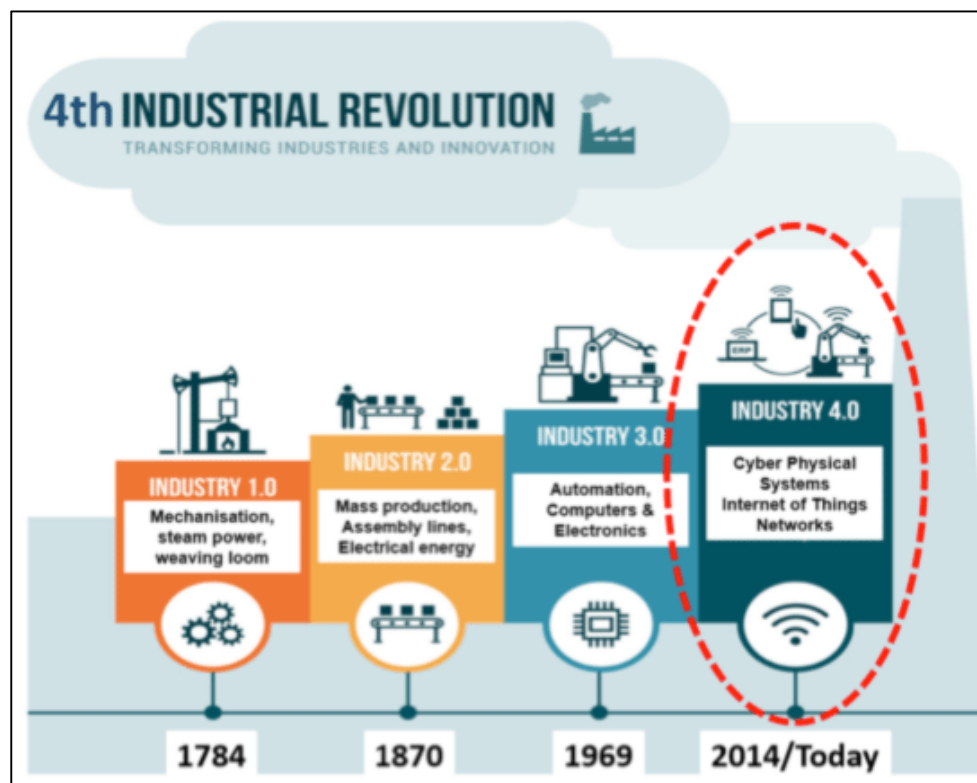


Figure 0.1 The timeline of the Industrial Revolution
Taken from BFPA (2017)

This rapidly growing technology of IoT combines sensors and electronics (Figure 0.2). The information from the physical system is collected by sensors to be then managed and processed locally. Then this information is sent to the application layer through the network layer for the implementation in their respective fields such as home, health, transportation, and others. Accordingly, we started hearing about smart portable medical devices, smart homes, and many

other examples. The success of this technology depends on the development of both sensors as well as electronics.

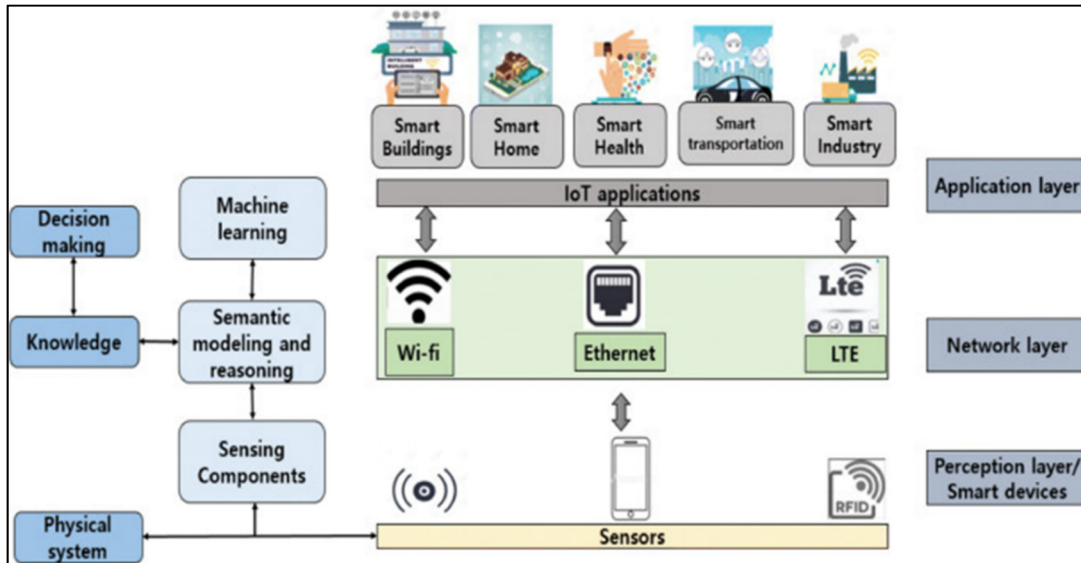


Figure 0.2 Overview of IoT Architecture
Taken from Phuyal et al. (2020)

Since access to IoT is mostly limited to advanced electronic devices, the addition of widespread sensors to the system is the first brick, which is the reason for the importance of producing more chemical and material-detecting sensors and developing low-profile robust wireless networks. If some advanced chemical and gas sensors become part of the IoT, such facilities could experience a giant leap forward (Gligoric et al., 2019).

On the other hand, printed electronics have sparked considerable interest in recent years due to their low e-waste generation, ease of fabrication, and potential for large-scale development of multifunctional devices. Various printing innovations have evolved over the years to pattern flexible surfaces in developing a variety of electronic devices. Additionally, Printable electronic inks materials provide an appealing platform for manufacturing and developing electronic devices and circuits for applications such as sensors, smart bandages, e-paper, and labels in various industries, including wearables, advertising, food packaging, and biomedical applications (Suganuma, 2014).

CHAPITRE 1

LITERATURE REVIEW

1.1 Sensors

As the industry evolves, reinvention of higher technology and devices is required. Real time monitoring and better sensing performances could accelerate and play a critical role in ensuring that industrial operations stay competitive and efficient. Therefore, by having a digitally interconnected systems powered by sensors and sensing devices will bring the ability to monitor and adapt changes continuously in situ.

1.1.1 History of Sensors

The invention of the miner's flame lamp by *Sir Humphrey Davy* in 1815 (Davy Lamp, (Figure 1.1) resulted in mine workers' safety and registered his name in history (Henry Pohs, 1995). Perhaps he did not know that he marked a turning point in human life with the introduction of this lamp. A wick lamp with a flame contained in a lattice plate makes up this lamp. The screen serves as a fire retardant barrier. Air (and any available fire retardant) can freely pass through the grid, but the holes are too small to allow flame to ignite and any fire outside this lattice plate (Henry Pohs, 1995), (James, 1994).

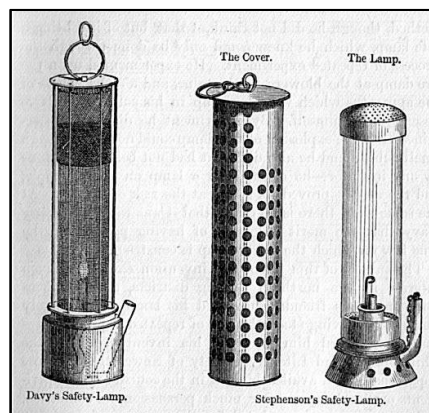


Figure 1.1 The Davy and Geordie lamps are safety lamps for use in flammable atmospheres like coal mines, invented in 1815 by Sir Humphrey Davy and George Stephenson
Taken from Henry Pohs (1995)

A year later, *George Stephenson* improved the lamp on two tenets: 1) The burning firedamp moved at a slow speed and 2) "burnt air" (carbonic gas, CO₂) would keep explosions from spreading (Henry Pohs, 1995). These lamps could be the spark of the invention of gas sensors, the invention day of sensors could go earlier than those days like Litmus paper for pH sensing (1800) and the thermometer (1612) (Dincer et al., 2019). Figure 1.2 shows a brief history line for sensors development (Dincer et al., 2019).



Figure 1.2 The discovery and development of various sensors over time are depicted in this timeline to materials (green), sensor technologies (blue), and biotechnology (black)
Taken from Dincer et al. (2019)

1.1.3 Classification of Sensors

Each sensor has a different operating concept based on the physical design and the physical parameter being measured. All sensors have one common: they transform a physical quantity (such as humidity) into a readable signal such as electrical, optical, acoustical, etc.

Sensors can be classified in many ways, depending on the type of output signal or the physical parameters they measure or considering particular circumstances that affect result collection. But, in general, and by their working mechanism, they could be divided into active and passive categories. An active sensor is a sensing device that an external source must power. In contrast, passive sensors can monitor and react to the signals from the external surroundings. The other classification form focuses on the sensor's detection method, such as chemical, electric, radioactive, biological, and other detection methods. The converting phenomena, i.e., the input and output, is the basis for another classification like thermo-optic, electrochemical, photoelectric, electromagnetic, or thermoelectric. Analog and digital sensors could be termed a division. Analog Sensors generate an analog output, a continuous output signal (generally voltage, and other quantities such as resistance, etc.) related to the quantity being measured. In comparison, digital sensors work with precisely defined or digital data. The data in digital sensors, which is used for converting and transmitting, is of the digital variety (Stefan et al., 2004).

1.1.4 Type of Sensors

Various sensors have been developed and manufactured based on application and necessity and can be classed using the previously described classification. Almost all IoT applications and electronic equipment contain at least a couple of sensors that provide feedback for physical property. Considering the desired parameter to measure with additional factors like accuracy and budget can lead to choosing, assigning, and employing the best sensor for any intended application. Sensors are: humidity sensor, Pressure sensor, Temperature sensor, Light sensor,

Gas sensor, Accelerometer, Touch sensor, Colorimetric sensor, Magnetic sensor (Hall Effect sensor), and Ultrasonic sensor.

1.1.5 Humidity Sensor

Based on the measurement techniques, humidity parameters are classified into relative and absolute humidity (Farahani et al., 2014). Absolute humidity (AB) units are used for the primary measurement in which H₂O content is measured. It is determined from the ratio of the mass of H₂O in gaseous environments to the volume of the gas (Farahani et al., 2014). Primarily, it is used for tracing moisture measurement as a primary humidity (Z. Chen & Lu, 2005)(Kulwicki, 1991). Relative humidity (RH) is temperature-dependent and classified as a secondary measurement of humidity (Farahani et al., 2014). It defines the ratio of the humidity content of air to the maximum humidity at a given temperature and pressure of the gas. Compared to AB sensors, RH sensors are the most frequently used in industry or individually because they have a simple design process and are cost-effective (Kulwicki, 1991). Humidity sensors have been in development for decades based on various hygroscopic sensing materials. Such sensors can either depend on physisorption or chemisorption mechanisms to monitor humidity (Mujumdar, 1987).

1.1.6 Classification of Humidity Sensors

Figure 1.4 shows that humidity sensors can be classified based on the type of the sensing material and their operating principle. Chen et al. (Z. Chen & Lu, 2005) classified sensors based on the sensing materials to ceramic, semiconductor, and polymer humidity sensors. Yamazoe et al. (Yamazoe & Shimizu, 1986) modified Chen's sensor classification to electrolytes, organic polymers (impedance, capacitance-type), and porous ceramics. Rittersma et al. (Rittersma, 2002)(Lee & Lee, 2005) classified humidity sensors into capacitive, resistive, hygrometric, gravimetric, and optical humidity sensors based on the sensing principles. Recently, humid sensors are classified into ceramic, resistive (ionic, electronic type),

capacitive, Polymer-based, surface acoustic waves (SAW), optical, mechanical, piezoelectric, thermal conductivity humidity sensors (Yadav, 2018).

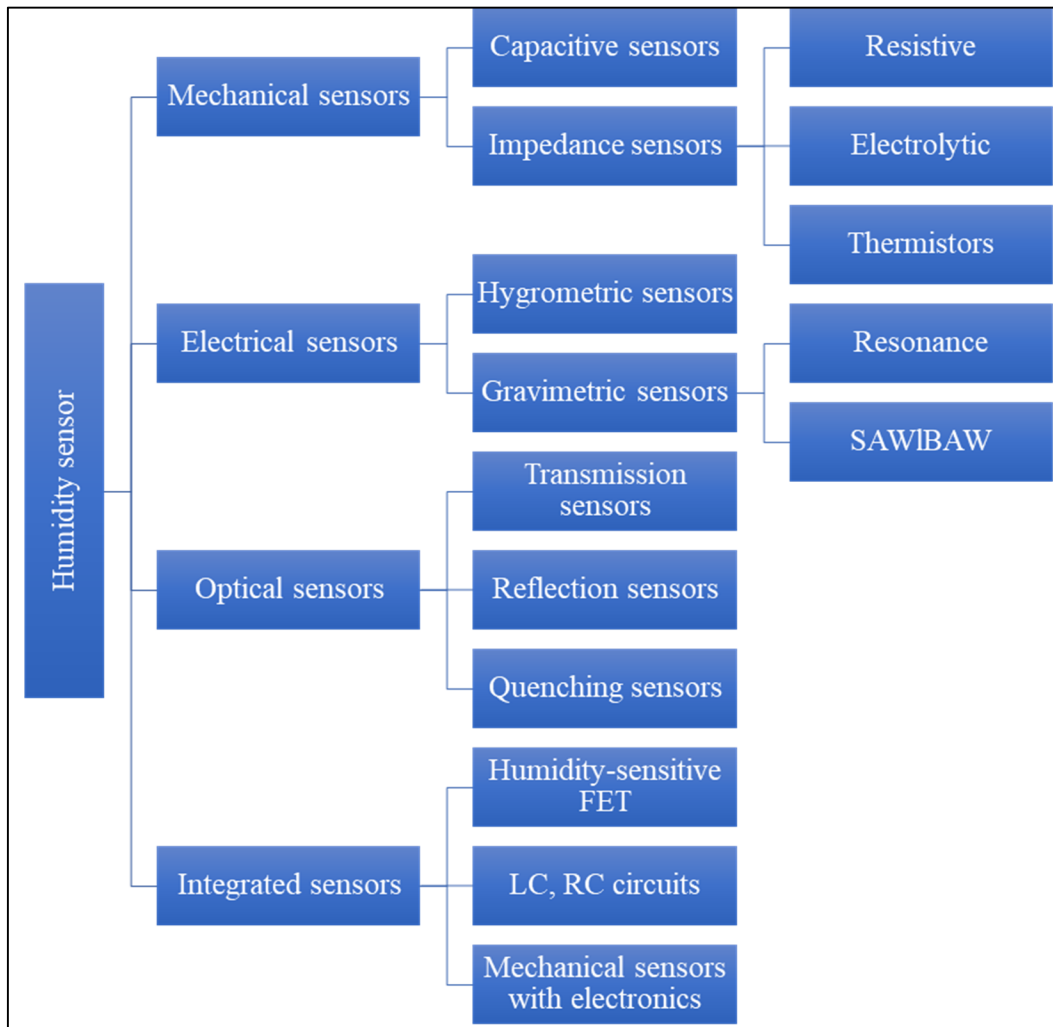


Figure 1.4 Humidity sensors classification based on the design and used techniques
Taken from Sikarwar & Yadav (2015)

Figure 1.5 classifies humidity sensors based on the type and the sensing principle (Sikarwar & Yadav, 2015). Among all, capacitive and resistive sensors are commonly used in humidity measurement techniques (Ertu, 2012). In contrast, resistive sensors depend on the impedance change caused by adsorbing humidity on the sensor's surface (Stefan et al., 2004). Capacitive sensors depend on the change of the dielectric constant related to absorbing humidity on their

bulk (Decaens & Vermeersch, 2016), changing the capacitance for sensors. Typically, capacitance linearly increases with increasing humidity (Stefan et al., 2004). Mainly, cellulose eaters and polyimide resins are used in the capacitive sensors.

Resistance-type humidity sensors use hygroscopic materials. These materials can show changes in their electrical resistance to humidity's adsorption/desorption process on the surface. In cyclic environments of dry and humid air, sensing materials can adsorb water in the presence of humidity and loses it in dry conditions in a repeatable way (Montgomery & McDowall, 2008). Common sensing materials employed in resistive sensors are ceramics (Al_2O_3 , SiO_2) (Z. Chen & Lu, 2005), semiconductors (TiO_2 (Sun et al., 2009), SnO_2 (Kuang et al., 2007), ZnO (Ates et al., 2013)); polymers (MAJEWSKI, 2016), 2D materials (Zhao et al., 2017), black phosphorus (Yu et al., 2020), and carbon materials (carbon nanotubes, and graphene) (Lv et al., 2019).

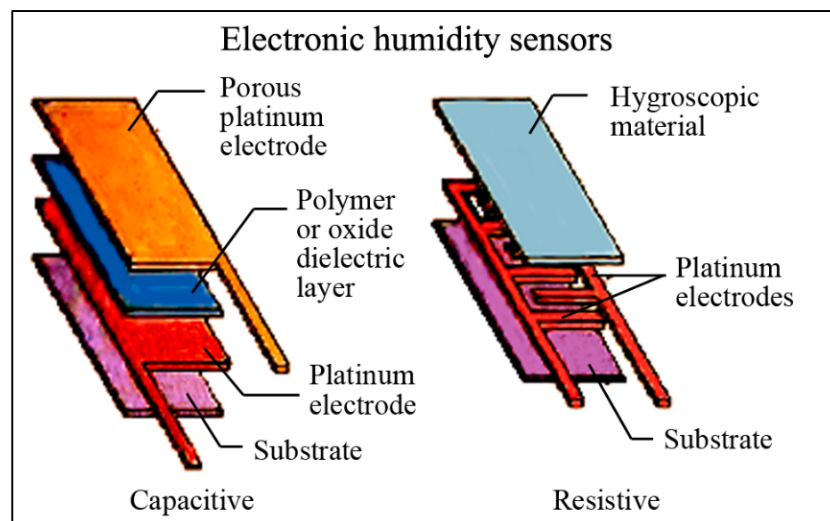


Figure 1.5 Capacitive and resistive humidity sensors
Taken from Ertu (2012)

1.2 Printed Electronics

Printed sensors and flexible devices are rapidly emerging into the industry. Therefore, the market for completely printed sensors is expected to reach \$4.9 billion by 2032. As a result of the development of numerous new applications and technologies, the overall category's market expansion is facilitated. There are numerous variables driving the adoption of multiple kinds of printed/flexible sensors. The increasing use of 'IoT' and 'Industry 4.0' is crucial, as they will necessitate huge networks of frequently wirelessly connected low-cost and unobtrusive sensors. Furthermore, the thin-film form factor and conformality of printed/flexible sensors allow them to be included within smaller devices, giving designers more opportunity to differentiate their products and perhaps new use cases (Dyson, 2021).

1.2.1 Review

Printed electronics (PE) are in continuous development since 1950s (Suganuma, 2014). Numerous involvement and efforts of many researchers and engineers through decades resulted in the discovery, development methods, and tremendous advancements in the twentieth century. PE is a platform that combines electronics fabrication with text and schematic printing. With such technology, it is possible to create high quality electronic components that are thin, flexible, stretchable, portable, of various sizes, and cost-effective (Suganuma, 2014).

A variety of printing methods have already been used in traditional electronics fabrication. Aerosol-jet printing (AJP), screen-printing, ink-jet printing, gravure printing, flexography printing, and offset printing are among them. Table 1.1 presents a comparison between different types of printing methods (Helmut Kipphan, 2001).

Table 1.1 Comparison between the printing technologies
Taken from Kipphan (2001)

Printing process	Transfer method	Drop Size / applied Pressure	Dynamic viscosity	Ink thickness on a substrate	Notes
Offset printing	Rollers	1 MPa	40–100 Pa·s	0.5–1.5 μm	High print quality
Rotogravure	Rollers	3 MPa	50–200 mPa·s	0.8–8 μm	Thick layers possible, excellent image reproduction,
Flexography	Rollers	0.3 MPa	50–500 mPa·s	0.8–2.5 μm	High quality (now HD)
Letterpress printing	Platen	10 MPa	50–150 Pa·s	0.5–1.5 μm	Slow drying
Screen-printing	Pressing ink through holes in the screen		1000–10,000 mPa·s	< 12 μm	Versatile method, low quality
Liquid electrophotography	Image formation by Electrostatics				excellent image reproduction, very thin image
Electrophotography	Electrostatics			5–10 μm	Thick ink
Ink-jet printer	Thermal	5–30 picolitres (pl)	1–5 mPa·s ^[37]	< 0.5 μm	Special paper required to reduce bleeding
Ink-jet printer	Piezoelectric	4–30 pl	5–20 mPa s	< 0.5 μm	Special paper required to reduce bleeding
Ink-jet printer	Continuous	5–100 pl	1–5 mPa·s	< 0.5 μm	Special paper required to reduce bleeding
Transfer-print	Thermal transfer film or water release decal				method of applying an image to a curved surface
Aerosol-jet printer	Aerosolized inks carried by the gas	2–5 microns in diameter	1–1000 mPa s	< 1 μm	Good printing resolution, High quality

1.2.2 Aerosol-Jet Printer (AJP)

In contrast to other printing techniques, AJP is a newer enhancement to the printing suite of tools and is being used in academic studies for upwards of a decade in various rallies. AJP, on the other hand, has considered a highly effective method for microscale digital printing technology using functional nanoparticles inks. Whereas the academic community has indicated credible capabilities in the latest years, Scientific analyses are used to promote inks and processing parameters. This has resulted in general qualitative standards and correlations for both ink and machine (Secor, 2018).

In AJP, liquid inks containing solvents and dispersed nano particles are atomized and forwarded to the medium surface by a carrier gas, deposited with great precision. Because it is contactless, printable, and observable simultaneously, and easy to fabricate patterning, AJP has synergistic advantages over many traditional methods and is being used in applied research fields such as transistor fabrication, complex circuits boards, and photovoltaic metallization.

It brings many benefits; AJP has a few downfalls that are excellently known to everyday users. Even though the process tolerates a wide range of inks, defining optimal print parameters is frequently a delicate process. In this regard, consistency and replication are challenging to achieve. They may necessitate drastic measures, such as frequent ink observation and replacement, optimization printing parameters for a specific ink that does not usually translate to new materials, nuzzle blocking, and spattering ink over the substrate (Secor, 2018).

1.3 Graphene and Sensors

Since the discovery of graphene, known as a magical material, it has been researched extensively due to electrical, mechanical, and chemical (Lau & Hui, 2002). Graphene is a single-layer sheet with sp^2 hybridized carbon atoms (Jarosz et al., 2016) produced by methods summarized as top-down or bottom-up methods (Figure 1.6). In this sheet, the in-plane δ bond is one of the strongest bonds, and the out-of-plane is the π bond, which creates a delocalized

network resulting in electron conduction. It exhibits a semi-metal feature with a zero-band gap, different from the metallic behavior of graphite (Chernozatonskii et al., 2006). Graphene has a specific surface area ($2630 \text{ m}^2 \text{ g}^{-1}$) and thermal conductivity ($5000 \text{ Wm}^{-1} \text{ K}^{-1}$) (Tung et al., 2017). Single-layer graphene has an optical transmittance up to 97.7% with a low sheet resistance of $30 \Omega \text{ sq}^{-1}$ (Ma & Zhi, 2019). It has excellent mechanical properties, higher than steel's tensile strength, which could be used in flexible, stretchable. Therefore it had strongly nominated for the development of wearable electronics (Lv et al., 2019) (Bhuyan et al., 2016). Accordingly, It has attracted attention to various applications, including electronics, optoelectronics, and chemical sensors (Bhuyan et al., 2016).

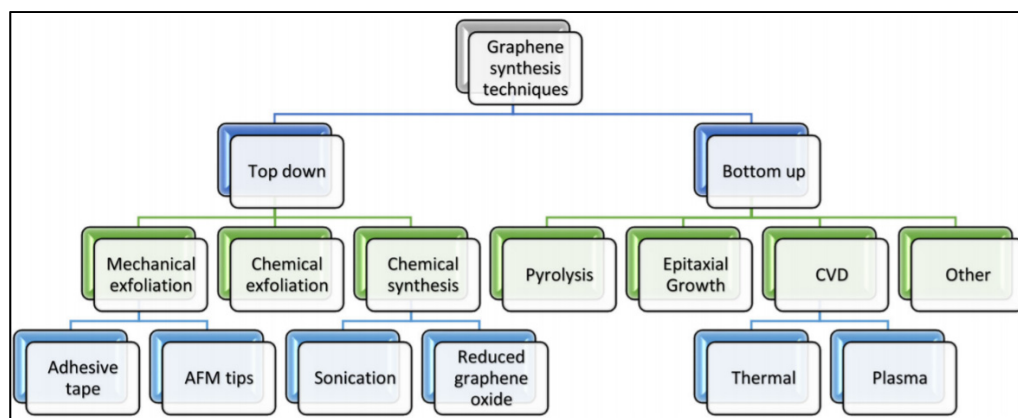


Figure 1.6 The different processes of Graphene synthesis
Taken from Bhuyan et al. (2016)

Graphene has been found a promising sensing material for humidity due to its high electron mobility, high specific surface area, and low electrical noise (Lv et al., 2019). Typically, in resistive sensors based on graphene, H_2O molecules will adsorb onto the graphene surfaces upon exposure to a humid environment. This causes a change in the electrical resistance of the graphene, which is proportional to humidity. Consequently, RH can be determined by measuring the changes in the electrical resistance $R_{\text{H}_2\text{O}}/R_{\text{air}}$. Significantly, sensors resistance can increase or decrease depending on the graphene derivative; pristine graphene, graphene oxide (GO), or reduced graphene oxide (rGO). Also, H_2O molecules' interaction with graphene is tricky. Whereas H_2O can withdraw electrons from pristine graphene, increasing the holes'

concentration and conductivity in flakes (C. Chen et al., 2018; Khalifa et al., 2020; Schedin et al., 2007; Shojaee et al., 2018). This results in a resistance reduction upon exposure to humidity. They can donate electrons to GO, and rGO leading to the opposite observation indicated for pristine graphene. Thus, a resistance elevation can be observed for sensors based on GO and rGO upon exposure to humidity.

Figure 1.7 shows a schematic illustration of a humidity resistive sensor that consists of a sensing material between two conductive electrodes on an inert substrate. The electrodes have an interdigitated structure to improve the sensing area and sensitivity. The graphene can be deposited onto the substrate with patterned electrodes by spin-coating, spray-coating, dip-coating, drop-casting, and printing (Wassei & Kaner, 2010). The sensitivity of graphene-based humidity sensors can be improved by increasing surface areas or adding functional groups sensitive to water molecules (Lv et al., 2019).

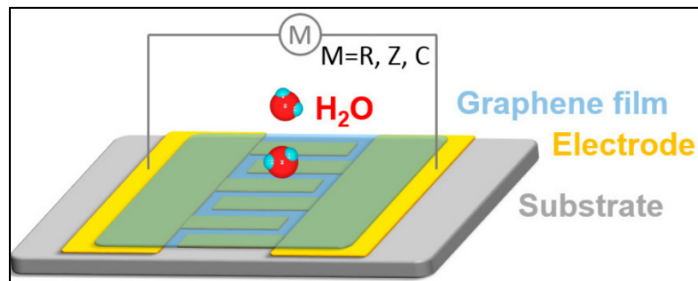


Figure 1.7 Graphene-based resistive humidity sensor
Taken from Lv et al. (2019)

1.3.1 Resistive Sensors Based on Graphene

Andric et al. (Andrić et al., 2021) fabricated chemiresistive graphene-based humidity sensors on PET and ceramic substrates. The graphene sensors, which were approximately 80% transparent, showed resistance fluctuations of up to 10% with increasing humidity, linear performance over RH ranging from 8% to 95%, and response times of 30 ms. Jeong et al. (Y. Jeong et al., 2021) investigated the humidity detection properties of an ink-jet printed sensor based on graphene quantum dots (GQDs), which were deposited locally on the interdigitated

CG-FG area (floating-gate (FG) interdigitated with control-gate (CG)). The humidity sensor responded to RH from 17.5% to 81.3%, with a response of 78% for RH \approx 81.3%. Hajian et al. (Hajian et al., 2020) fabricated a resistive humidity sensor based on fluorinated graphene (FG) solution over silver (Ag)-based interdigitated electrodes (IDEs) screen-printed on a flexible polyimide substrate. The FG-based humidity sensors exhibited a 13.3% change in the relative resistance, a sensitivity of 0.22%/RH, and response/recovery times of 82 s / 125 s, when the RH changed from 20% to 80%. Table 1.2 summarizes further examples for graphene-based chemiresistive humidity sensors.

Table 1.2 Comparison of graphene-based chemiresistive humidity sensors
Adapted from Barmpakos & Kaltsas (2021)

Active Material	Electrodes	Substrate	(%RH)	Sensitivity	Ref.
Gravure printed MWCNTs	Screen-printed, Ag	PI	30–60	0.96% /%RH	(X. Zhang et al., 2019)
Gravure printed MWCNTs	Screen-printed, Ag	PI	10–90	–	(Xingzhe Zhang et al., 2020)
Drop-cast TiO ₂ nanoflowers	Gravure, Ag	PI	20–95	485.7 /RH%	(H. Jeong et al., 2019)
Screen-printed MEPAB/ CMDAB/MMA copolymer	Screen-printed, Ag/Au	PI	20–95	0.0586 logW /% RH	(M.-J. Kim & Gong, 2012)
Screen-printed epoxy/IPN polyelectrolyte	Chemical Etching Plating (Ni/Au)	PI	20–95	0.046 logW /% RH	(Lim et al., 2013)
Drop-cast SnO ₂ /rGO	Chemical Etching Plating (Cu/Ni)	PI	11–97	15.19–45.02%	(D. Zhang et al., 2016)
Spin-coat PEDOT:PSS (15%) + PVA (SAW)	Photolithography	LiNbO ₃	0–80	350 W /% RH	(Choi et al., 2015)
Spin-coat PEDOT:PSS (5 wt%) + ZnSnO ₃ (5 wt%)	Photolithography, Au	LiNbO ₃	0–90	–	(Aziz et al., 2015)

Table 1.2 Comparison of graphene-based chemiresistive humidity sensors
Adapted from Barmpakos & Kaltsas (2021) [Continued]

Active Material	Electrodes	Substrate	(%RH)	Sensitivity	Ref.
Screen-printed MDBBAC/MMA (70/30) Polyelectrolyte	Screen-printed, Ag-Plating (Cu/Ni/Au)	Glass Epoxy	20–95	0.0349 logW /% RH	(Ahn et al., 2012)
EHD Graphene/methyl	Ink-jet-printed, Ag	PET	5–95	96.36%	(Ali et al., 2016)
Drop-cast Pt/MoS2 (0.25:1)	Photolithography, Au	Ceramic	35–85	85 % RH	(Burman et al., 2018)
Gravure printed CNT	Screen-printed, Ag	PET	20–80	0.1% /% RH	(V. S. Turkani et al., 2018)
Screen-printed TiO2-Cu2O-Na2O	Screen-printed, Pt	Al2O3	20–95	–	(D.-U. Kim & Gong, 2005)
Ink-jet-printed PANI	–	Polyester	20–96	–	(Kulkarni et al., 2012)
Micro-pipette deposited Nafion	Screen-printed, Ag on PU	Polyester cotton	30–90	–	(Kutzner et al., 2013)
Gravure printed FMWCNT/HEC (1:6 w/w)	Screen-printed, Ag	PET	20–80	0.048 /% RH	(Vikram S. Turkani et al., 2019)
Ink-jet-printed PEDOT:rGO-PEI/Au NPs	–	PET	11–98	7.41–51.60%	(R. Zhang et al., 2018)
Spin-coated Fe2O3	Ink-jet-printed, Ag	PET	0–100	~88.89%	(Khan et al., 2020)
fluorinated graphene (FG)	Screen-printed, Ag	flexible polyimide	20-80	0.22% RH	(Hajian et al., 2020)
graphene quantum dots (GQDs)	Ink-jet-printed, Ag	Sio2	17-81	30-40%	(Y. Jeong et al., 2021)
liquid phase exfoliated graphene	interdigitated electrodes	PET, ceramic	8-95	5%RH	(Andrić et al., 2021)
Aerosol printed graphene (LPE)	Screen-printed, C	PET	22-90	0.55%	

1.3.2 Graphene Inks

Elevated ink advancement has piqued the interest of emerging printed and flexible devices for industrial and commercial applications. Graphene-based inks have incredibly become the most researched as a key player in this area owing to their excellent properties such as, but not limited to, excellent conductivity and mechanical strength. Furthermore, graphene has demonstrated a high potential for engineering (for example, chemical and physical functionalization, coating metals, and so on), letting the characteristics of graphene be controlled and adapted to a wide range of devices. As a result, researchers thoroughly investigated their use as an alternative to conventional materials in various applications.

Currently, polar and high-boiling-point solvents are used to make inks, such as N-methyl-2-pyrrolidone (NMP) (B. Liang et al., 2021), dimethylformamide (DMF) (Tkachev et al., 2021), cyclohexanone (Barmpakos et al., 2021), terpineol (D. S. Kim et al., 2021), toluene (Htwe et al., 2021), and tetrahydrofuran (THF)(Salavagione et al., 2020). Graphene has a surface energy of $46.7 \text{ mJ}\cdot\text{m}^{-2}$ and Hansen solubility parameters (HSPs) of 18, 12.3, and 7.2 $\text{MPa}^{1/2}$ for the dispersive (D), polar (P), and H-bond (H) parameters, respectively. (A. Al Shboul et al., 2017; A. M. Al Shboul et al., 2018; Hernandez et al., 2010). The solvents mentioned above were efficient in formulating dispersant-free graphene inks relying on the close match between their surface tension ($33\text{-}48 \text{ mN}\cdot\text{m}^{-1}$) and the HSPs ($17\text{-}18 \text{ MPa}^{1/2}$ for D, $5\text{-}12 \text{ MPa}^{1/2}$ for P, and $5\text{-}26 \text{ MPa}^{1/2}$ for H parameters) to those for graphene. Knowing that additives (ex. Polymers) can negatively impact graphene films' electrical properties (A. Al Shboul et al., 2017), these solvents are ideal for preparing colloidally stable free-additives graphene inks.

However, these solvents are not without issues. As a result of the slow evaporation rate, the energy consumption, toxicity, and contribution to greenhouse gas emissions (Byrne et al., 2016), scientists pursued their endeavors to develop conductive graphene inks using more suitable and/or green solvents while keeping devices functioning. To address the issues mentioned earlier and promote public/environmental health, researchers are working to reduce

solvent consumption or replace it in ink composition with greener options (Kamarudin et al., 2021).

Water is the best environmentally-friendly green solvent for boosting green chemistry in electronics manufacture (Hartonen & Riekkola, 2017). Water's valuable role as a solvent is related to its characteristics, such as high abundance, low-cost, non-flammability, and zero health impact (Filly et al., 2016). However, water and graphene are not soluble because of the surface energy and surface tension of water (72.7 mJ.m^{-2}) (Carl L. Yaws, 2008; Shin et al., 2011; The Chemical Rubber Company, 1969), far from the one for graphene (46.7 mJ.m^{-2}) (Wang et al., 2009). Additives were used to balance the surface energy between graphene and water. In this work, biocompatible dispersants such as gelatin, triton X-100, and tween 20 were employed in the graphene inks' formulation intending to exclude harmful materials. As a result, green graphene inks were produced, leading to green sensors that prevent releasing harmful materials to the environment or contact vital subjects such as human skin.

In developing green graphene inks, Chen et al. (H. Chen et al., 2021) develop multipurpose graphene aqueous inks with high conductivity based on sand-milling exfoliation of raw graphite for screen-printing. This method produces 62.8% graphene dispersed in water at high concentrations of up to 25.1 mg.mL^{-1} for application in supercapacitors and heaters. The graphene layer exhibits a fast-ramping temperature ($171.9 \text{ }^\circ\text{C}$) at 8 V in 75 s in the heating device and high areal capacitance (1.36 mF.cm^{-2}) in the MSCs due to its outstanding conductivity (up to 870 S.cm^{-1} after annealing). In another approach by Htwe et al. (Htwe & Mariatti, 2021), graphene conductive inks were synthesized by combining deionized (DI) water with several surfactants (SDS, PVP, and GA) for ink-jet printing technique. The film was printed on a PET with a $125 \text{ }\mu\text{m}$ thickness for wearable electronics. In this research, when the bending force was released after 100 bending cycles, the initial electrical conductivity of $5.2 \times 10^3 \text{ Sm}^{-1}$ only decreased by roughly 0.2 percent. Nayak et al. (Nayak et al., 2021) formulated the graphene solution using ethanol and water by LPE technique and created a conductive graphene ink with no coffee ring formation for practical ink-jet printing. The film's resistivity was measured at $200 \text{ }^\circ\text{C}$ to be $35 \text{ }\Omega\text{-cm}$, which drops to $1.06 \text{ }\Omega\text{-cm}$ when the

temperature is raised to 300 °C. Table 1.3 provides more examples for aqueous graphene inks, besides the inks formulated in low-harmful solvents such as IPA and ethanol.

Table 1.3 Selected examples of the graphene-based inks and their printable applications
Adapted from Hu et al. (2018)

	Solvents	Binders & additives	Substrates	Applications	Ref.
Ink-jet inks					
Graphene	IPA	–	PET, Polyurethane	FETs	(Carey et al., 2017)
Graphene	Water /Ethanol	–	PET	Conductive inks	(Capasso et al., 2015)
Graphene	Water /Ethanol	–	Si/SiO ₂	–	(Bianchi et al., 2017)
Graphene	Water	SDBS, PANI	Carbon	Supercapacitors	(Y. Xu et al., 2014)
Graphene	Water	PEDOT: PSS	Carbon	Gas sensors	(Sriprachubwong et al., 2012)
Graphene	Water	PS1	Si/SiO ₂	Photodetectors, memory	(McManus et al., 2017)
Graphene	IPA, NMP, Terpineol /CHO	Ethyl cellulose	PET	Photodetectors	(Hossain et al., 2017)
Graphene	IPA	PVP	Si ₃ N ₄	Humidity sensors	(Santra et al., 2015)
Graphene	IPA	PVP	FTO glass	Solar cells	(Dodoo-Arhin et al., 2016)
Graphene	IPA	PVP	Kapton, glass	Thermoelectrics	(Juntunen et al., 2018)
Graphene	IPA/n-butanol	Plasdone S-630	Paper	Conductive inks	(Arapov et al., 2014)
Graphene	Terpineol /Ethanol	Ethyl cellulose	Si/SiO ₂ , glass	FETs	(Li et al., 2013)
Graphene	Ethyl lactate/octyl acetate	Nitro-cellulose	Glass, Kapton	Conductive inks	(Secor et al., 2017)
Graphene	Diethylene glycol /Ethanol	PEDOT: PSS	Polyurethane	Temperature sensors	(Vuorinen et al., 2016)

Table 1.3 Selected examples of the graphene-based inks and their printable applications
Adapted from Hu et al. (2018) [Continued]

	Solvents	Binders & additives	Substrates	Applications	Ref.
Graphene	Water	SDS/ PVP	PET	Wearable electronics	(Htwe & Mariatti, 2021)
Graphene	Water /Ethanol	EG/EC	Glass, SiO ₂	Practical applications	(Nayak et al., 2021)
Flexographic inks					
Graphene	Water/IPA	Na-CMC	ITO PET	Solar cells	(Baker et al., 2014)
Gravure inks					
Graphene	Terpineol /Ethanol	Ethyl cellulose	Kapton	Conductive inks	(Secor et al., 2014)
Screen inks					
Graphene	Ethanol	PTFE, PANI	PET	Supercapacitors	(Y. Xu et al., 2013)
Graphene	Terpineol /Ethanol	Ethyl cellulose	Si/SiO ₂ , Kapton	Conductive inks	(Hyun et al., 2015)
Graphene	Water	Na-CMC	Glass, paper	Conductive inks	(Karagiannidis et al., 2017)
Graphene	Water/IPA /	CMC	PI/PET/Glass	Supercapacitors, Heaters	(H. Chen et al., 2021)

This work is divided into two sections. The first section is concerned with the synthesis and characterization of aqueous green graphene inks bound to biocompatible dispersants. The second section discusses how to use effective ink on production and sensing evaluation of printed and flexible humidity sensors.

CHAPITRE 2

METHODOLOGY

Concepts and techniques for methodical development of printed humidity sensors involving ink preparation, screen-printed electrodes, and sensor fabrication are identified in this section. The constructed hypothesis, test and experiment techniques, and data collecting are explained.

2.1 Materials

Graphite (7-10 μm) was obtained from alfa easer, triton X-100 was obtained from EMD-Millipore, BioShop Canada Inc. supplied tween-20, and gelatin was obtained from Sigma-Aldrich. Commercial carbon ink for screen-printing was provided from Loctite (LOCTITE EDAG 423SS E&C).

2.2 Preparation of Green Graphene Inks (GGe, GTr, GTw)

Three green graphene inks (GTr, GTw, GGe) were prepared using the direct liquid phase exfoliation (LPE) technique, as shown in Figure 2.1. Specifically, 1 g of graphite was ultrasonicated for 8 hours with an optimized quantity of 1 g triton X-100 in 1 L of distilled water. This process was repeated for the other two dispersants (tween-20 and gelatin) with quantities of 1.5 g for tween-20 and 0.1 g for gelatin. The dispersions were transferred into 250 ml centrifuge tubes and subsequently centrifuged at 14k rpm (12,400 g) for 2 hours to collect graphene flakes at the centrifuge tubes' bottom. The excess and unbounded dispersants in the supernatant were decanted from the aqueous dispersion. If the excess triton X-100 and tween-20 were not excluded from the graphene ink, experimentally, they could complicate solidifying the graphene films after printing related to the liquid nature of the dispersants mentioned above room temperature. However, this issue was settled by excluding the excess amount of these dispersants by decanting the supernatant after centrifugation at 14k and limit their presence in the graphene ink by the ones only adsorbed on the graphene's surface.

The graphene precipitations were then dispersed in 1 L for 1 hour. Subsequently, the dispersions were centrifuged twice at 1k (121 g) for 30 minutes to remove un-exfoliated graphite flakes and 14k (12,400 g) for 2 hours to exclude the small graphene flakes from the final inks' formulations. At the end of the 14k centrifugation, graphene flakes were collected at the centrifuge tubes' bottom. Finally, the graphene precipitations were sonicated in 100 mL pure distilled water for 1 hour, producing graphene inks with a concentration of 2 mg.mL⁻¹. Viscosity (1-10 cP) measured by SV10 viscometer (Malvern instruments) and concentration (2 mg mL⁻¹) of the ink by dilution were determined to adjust the physical properties for inks to ease their printability by using the AJP. The green graphene inks were indicated as pure graphene inks and referred to the dispersant used for the preparation; GTr refers to the ink prepared with triton X-100, GTw refers to the ink prepared with tween-20, GGe refers to the ink prepared with gelatin. These inks are environmentally-friendly due to avoiding toxic solvents in addition to the use of biodegradable polymers. Thus, the final product of inks should be eco-friendly that can release unharmed products upon degradation in the environment.

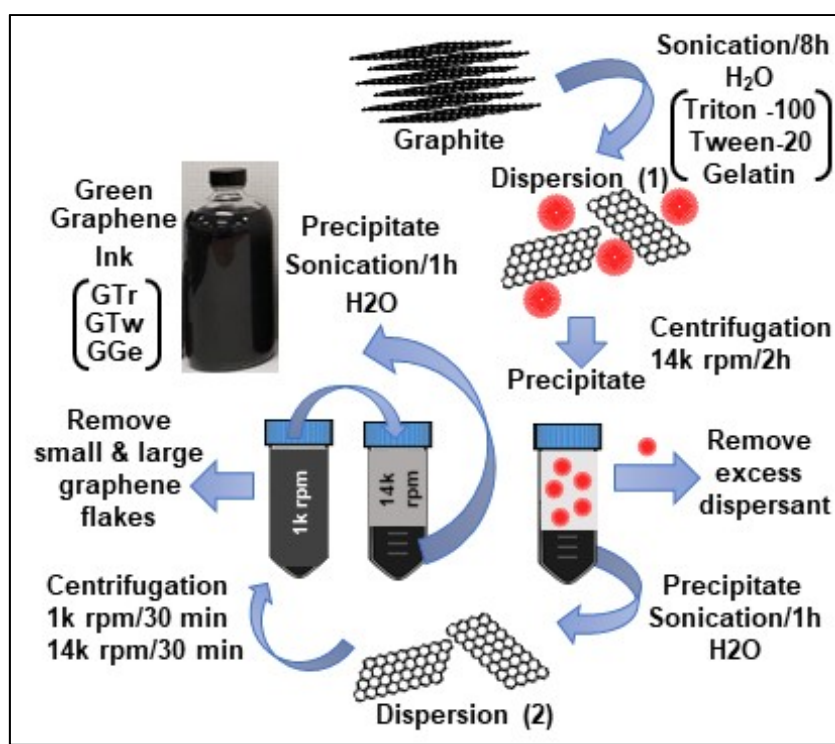


Figure 2.1 The preparation procedure for the green graphene inks; GTr, GTw, and GGe

2.3 Preparation of Gelatin-modified GTr Ink (Ge-GTr)

Modified GTr inks were prepared by simply dissolving the gelatin resin directly in the GTr inks. Various quantities of gelatin were stirred continuously overnight in the GTr inks, and the concentrations of gelatin in the modified inks were adjusted to 0.1, 0.25, 0.5, and 1 mg.mL⁻¹. The prepared inks were labeled as 0.1Ge-GTr, 0.25Ge-GTr, 0.5Ge-GTr, and 1Ge-GTr, respectively. These inks were considered to fabricate the graphene humidity sensors. Later, the other inks (GTw and GGe) and their modification will be considered for sensors fabrication in future studies. Here, gelatin is beneficial to (1) Elevate inks viscosity and their printability, (2) Enhance the mechanical strength for the printed films, and (3) enhance the humidity sensing detection for sensors.

2.4 Sensor Fabrication

Toward optimal printing performance for an AJP (Figure 2.2) should be fixed for ink characteristics (viscosity, concentration, stability). These parameters are essential to make an excellent and stable mist to have continuous and same quality print. The template and tube temperature, and printing speed are also important parameters. Therefore, a systematic study was carried out to find the best parameters to print graphene inks. These parameters include the bottle position, the longitude, the latitude, the bottle depth into the atomizer chamber, the atomizer power, the gas sheath, the nozzle pressure, the nozzle size, the height from a substrate, the ink volume in the bottle, and the printing speed.



Figure 2.2 X-Position and Angle Position, Atomizer water level, Aerosol-Jet Printer, Nozzle distance and Atomizer chamber and ink Tube

In this research, graphene films (5 mm x 5 mm) with various number of printing layers (Figure 2.3) were printed on top polyethylene terephthalate (PET) substrate using an aerosol spray printing (Optomec, Aerosol-Jet, USA) with a 300 μm diameter nozzle, and the carrier gas/sheath gas rates were fixed at 15 sccm/40 sccm. During aerosol-jet printing, the stage was maintained at 100°C, and the working distance was 46mm. The volume of the ink inside the bottle was 0.75mL. Later, graphene films were incubated overnight at 40 °C to ensure water removal.

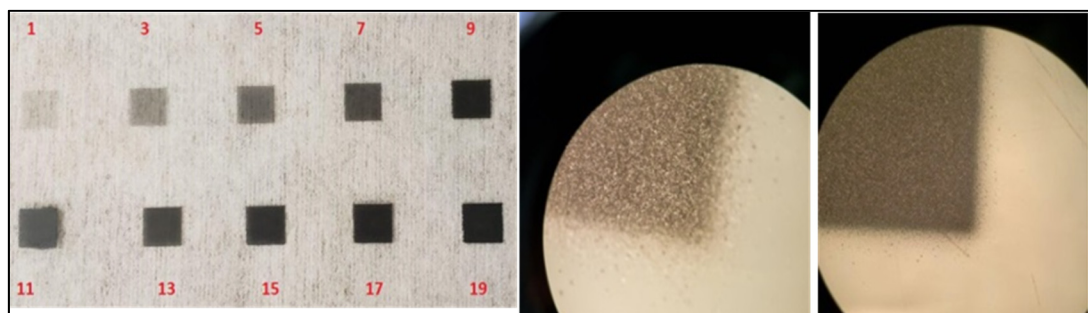


Figure 2.3 Printed GTr films with different printing passes on top PET substrate

The exact process was used to fabricate the graphene humidity sensors. The dimensions for the sensing graphene thin films were 1 mm length x 500 μm width x 400 nm thick. The electrical resistance was 200 k Ω in air ambient for the as-fabricated sensors (Figure 2.4).

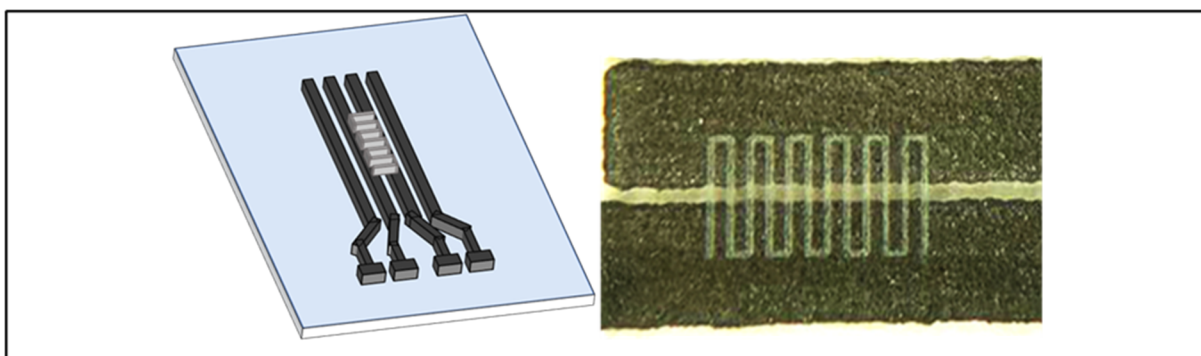


Figure 2.4 Printed GTr sensor on top screen-printed carbon electrodes pre-prepared on top PET substrate

Noteworthy, a systematic study was carried out to find the best printing pattern and electrode. Accordingly, we printed different patterns such as mesh, zigzag, and ladder (Figure 2.5). By reviewing the results of the pattern response analysis, it was found that in the mesh and zigzag pattern, the resistance decreases with increasing humidity, but remains constant or increases sharply after a while. This phenomenon could be explained because of sharp edges on zigzag and crowded network of mesh. Thus, upon exposure to humidity, H₂O molecules start accumulating on films surface leading to the reduction on sensors resistance until saturating the surface which cause the signal to stabilize. Further accumulation of H₂O molecules on films surface leads to create a pressure and eventually films can break and results in sudden increase in the resistance. Therefore, the ladder pattern showed the best performance (Figure 2.6).

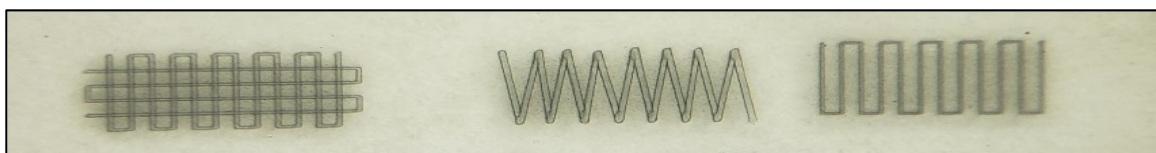


Figure 2.5 Mesh, Zigzag and Ladder Patterns

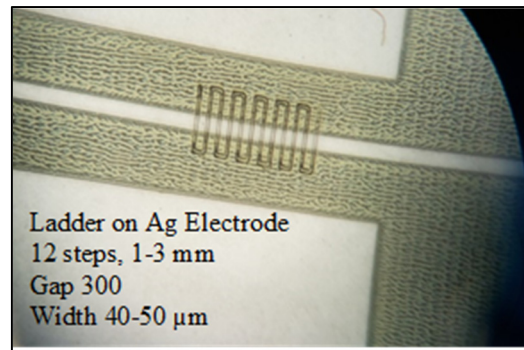


Figure 2.6 Sensing layer on Ag electrode

Later, we evaluated different electrodes, including silver (Ag), copper (Cu), and two types of carbon (C) electrodes. The metallic-type electrodes (Ag and Cu) were easily oxidized, leading to odd response signals. Figure 2.7 shows the analysis for graphene sensors printed on top of Cu, Ag, and two different kinds of C electrodes. Although, Ag and C electrodes showed promising results, but C electrodes were more stable than the Ag electrodes. Therefore, C electrodes were used for the rest of the study.

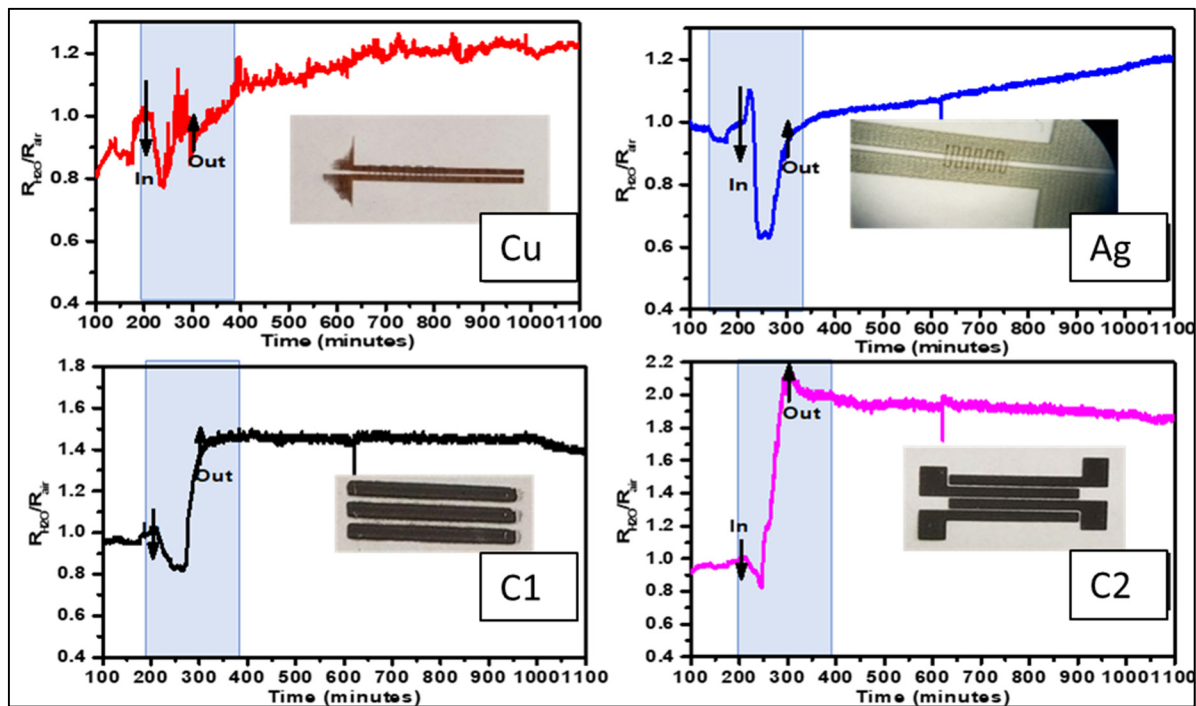


Figure 2.7 Cu, Ag and C electrodes

2.5 Preparation of Screen-printed C-electrodes

A commercial carbon paste (LOCTITE EDAG 423SS E&C) was obtained from Loctite and used to make the new C-electrodes for sensors fabrication. The designing of new electrodes was carried out by AutoCAD software and then transferred to screen-printing software. The mask for screen-printing was developed, and the electrodes were printed by KeKo P-200A machine at ETS. The dimensions for the screen-printed carbon electrodes were 1.5 mm length x 1 mm width x 5 μm thick, with 100 μm spacing between the carbon bars (figure 2.8).

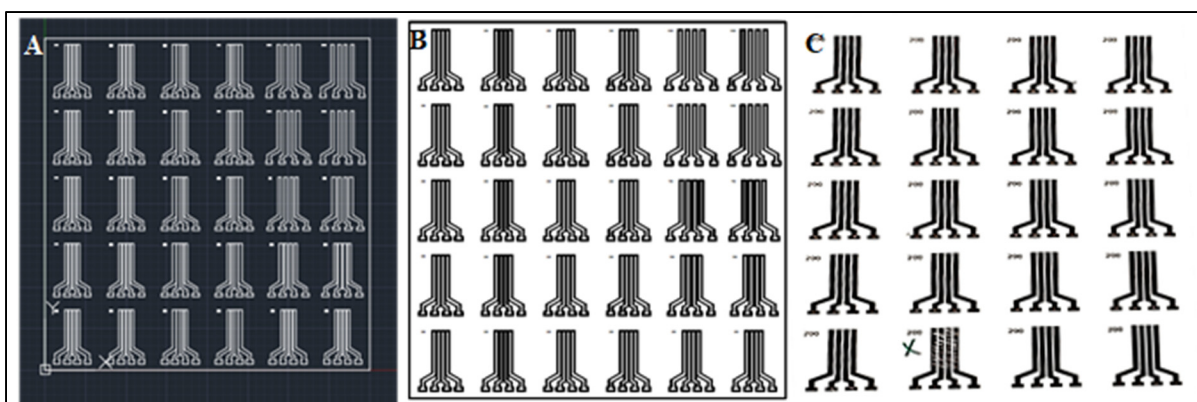


Figure 2.8 (A) Electrodes design by AutoCAD software, (B) Design used to create the mask for screen-printing, (C) Screen-printed electrodes

2.6 Data Collection

A portable and low-cost Arduino-based technique (Figure 2.9) was implemented to measure the Device Under Test (DUT) functionalities by transferring a generalized voltage through its ports and measuring the associated current flowing through it. The system collects DUT current-voltage signal and transmits it to a computer to process. The Arduino-based system accurately measures ohmic values, voltages and current. Despite the minor fluctuations, it is a feasible replacement for Keithley source Meter 2400 (Dogara et al., 2018).

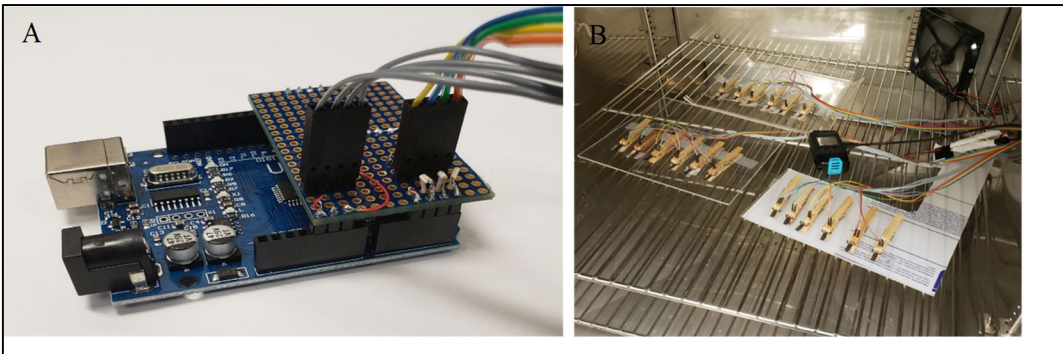


Figure 2.9 (A) Arduino device, (B) Series of sensors in ETS environmental chamber

The humidity and temperature control were achieved using an environmental test chamber (Tenney T10rc-1.5), as shown in Figure 2.10. The RH and temperature values were estimated using portable temperature/humidity data logger (Omega OM-EL-GFX-2-PLUS). The output signals generated for sensors were measured using a programmable multimeter connected to a PC via an Arduino card. The sensor response is defined as $(\Delta R/R_{air}) \times 100\%$, where ΔR represents the electrical resistance differences for sensors exposed to higher humidity and initial electrical resistance at $RH \approx 30\%$, respectively. Sensors sensitivity for humidity detection is defined as $(\Delta R/\Delta RH)$, where ΔR is the difference between the electrical resistance at high and low humidity levels. ΔRH is the difference between high and low humidity levels. The time taken by the sensor to reach 90% of the response represents the response and recovery times.

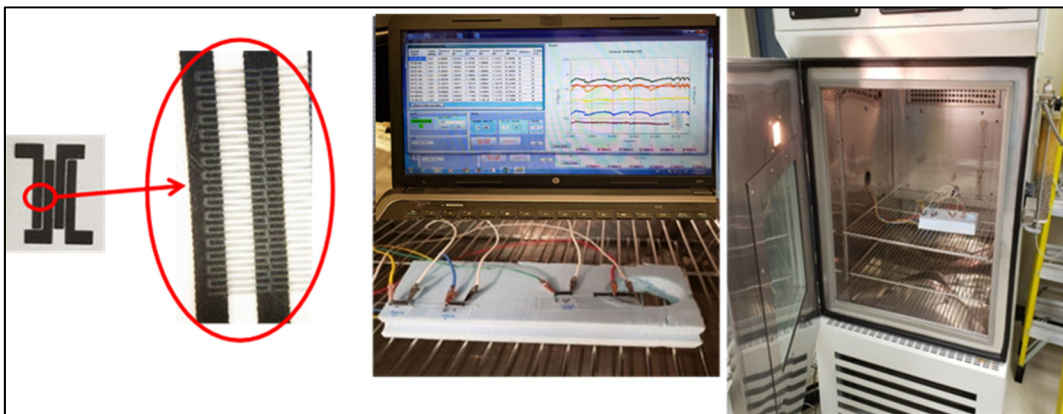


Figure 2.10 Sensors printed on carbon electrodes were taken to be tested with humidity at ETS by using the environmental chambers

2.7 Characterization

This work entails a variety of chemical and electrical characterization of inks and printed films. These methods were chosen to demonstrate and collect data as accurately as feasible. Because science is based on facts, it was attempted to develop a scientific approach for making a printed flexible graphene humidity sensor by aiming for quantifiable outcomes through testing and analysis, as well as by gathering measurable, empirical evidence along with hypothesis-related experiments.

2.7.1 Ultraviolet-visible Spectroscopy (UV-Vis)

UV-Vis is one of the most used diagnostic techniques because of its versatility and ability to detect nearly every molecule. The technique involves passing UV-Vis light through a sample and measuring the light transmittance. The absorbance (A) can be calculated using the transmittance (T) as $A = -\log(T)$. It can qualitatively recognize functional groups or verify the presence of a chemical by matching the absorption spectra. Since the analyte concentration is related to absorbance using the Beer-Lambert law (Equation 1), it can also determine materials' concentrations. Here, absorbance spectra were recorded by a UV-Vis spectrophotometer (Cary 100 Bio, Agilent Technologies, USA) using a quartz cell with a path length of 1 cm at room temperature. The graphene's concentration was calculated using an absorption coefficient (ϵ) of $24.6 \text{ mL}\cdot\text{cm}^{-1}\cdot\text{mg}^{-1}$ (A. Al Shboul et al., 2017), (Hernandez et al., 2010). for the absorption at a wavelength of 660.

$$Abs. = C * \epsilon * l \quad (2.1)$$

2.7.2 The Dynamic Light Scattering (DLS)

DLS (also known as Quasi-Elastic Light Scattering or Photon Correlation Spectroscopy) analysis was performed at the wavelength ($\lambda=633 \text{ nm}$) using particle size analyzer equipped with a 4mW laser and Avalanche photodiode detector (Malvern, Zetasizer Nano S90, UK).

Typically, DLS is a standard analysis technique to determine the particle size detection in the liquid phase with a diameter range of 0.3 nm – 5 μm . Polymers, micelles, emulsions, proteins, and nanoparticles are some examples of typical applications. In non-spherical particles like graphene, the scattering analysis assumes graphene flakes are spherical. Thus, it can be helpful to the approximate diameter size distribution of flakes in their dispersions. For DLS, the inks were diluted to 0.02 mg. mL^{-1} before the measurement.

2.7.3 Raman Spectroscopy

The graphitization degree for graphene was estimated from Raman spectra collected from 400 cm^{-1} to 4000 cm^{-1} with a Raman microscope (Renishaw, in Via Reflex., UK) at room temperature and 532 nm excitation laser. The characteristic Raman bands of carbon-based sp^2 materials are located around 1350 attributed to the D-band, 1580 to the G-band, 2700 to the D-band, and 2900 cm^{-1} to the D'-bands. The D-band is assigned to structural disorders, the G-band is related to the E_{2g} phonon of sp^2 carbon atoms, and the 2D band is a second-order two-phonon process. The average size of the sp^2 domains is proportional to the peak intensity ratio of the D and G bands (I_D/I_G), estimating the graphitization degree of graphene (i.e. degree of order in crystalline structures) (A. M. Al Shboul et al., 2018), (A. Al Shboul et al., 2017).

2.7.4 Atomic Force Microscopy (AFM)

AFM is a useful method for scanning almost any texture, including polymers, ceramics, composites, glass, and biological samples. Various properties such as adhesion strength, magnetic forces, and mechanical properties are measured and identified using AFM. It is equipped with a sharp tip with 10 to 20 nm diameter connected to a cantilever. The AFM is a tool for imaging and manipulating atoms and structures on various surfaces. When it forms incipient chemical bonds with each atom, the atom at the tip's apex "senses" individual atoms on the underlying surface. These chemical interactions can be identified and mapped because they gently affect the tip's vibrating frequency. AFM can be used in two fundamental modes: contact and tapping. In contact mode, the AFM tip is always in contact with the surface. The

AFM cantilever is vibrated above the sample surface in the tapping mode, allowing the tip to make only sporadic contact with the surface (Sinha Ray, 2013).

The morphology characteristics for graphene flakes were investigated by AFM (Bruker, MultiMode8, USA). AFM images were acquired in the tapping mode at ambient conditions for samples prepared by drop-casting a drop of diluted graphene solutions (0.2 mg.mL^{-1}) on a freshly cleaved mica piece. AFM samples were left overnight to dry at room temperature. Then they were then taken out for imaging.

2.7.5 Transmission Electron Microscopy (TEM)

The Transmission Electron Microscope is a widely used analytical technique in materials science, pollution, nanotechnology, and semiconductor research. The TEM functions on the same basic principles as a light microscope, except instead of light, it employs electrons. Because electrons have a much shorter wavelength than light, the ideal resolution of TEM images is many orders of magnitude higher than that of a light microscope. As a result, TEMs can unveil the tiniest features of a microstructure.

The samples' microstructure was investigated by transmission electron microscopy (TEM, JEOL JEM-2100F, Japan) equipped with a field emission gun-running at 200 kV. TEM samples were prepared from diluted graphene dispersions a $\sim 0.02 \text{ mg.mL}^{-1}$ concentration. Lacey grids (TED PELLA, USA) were dipped in the diluted dispersion and left to dry overnight at room temperature before the measurements.

2.7.6 Scanning Electron Microscope (SEM)

SEM is a type of electron microscope that scans the surface of a material with a focused stream of electrons to produce pictures. It provides access to analyze surface topography, and it can expose various stages of layer-by-layer deposited materials. The microstructures of the graphene films were observed by SEM (JEOL JCM-6000plus, Japan). SEM is vital for

researchers to visualize the specimen topography, microstructure, or even determine the cause of failure and microstructural defects of fabricated features at micro and nano dimensions.

2.7.7 Zeta-Potential

The zeta-potential is the potential difference between the dispersion medium and the stationary layer of fluid associated to the dispersed particle. In other words, it refers to the electric potential at the slipping plane. This plane is the interface that divides fluid that is mobile from the fluid that is still connected to the surface. As a result, zeta-potential is a key measurand for studying the repulsive interactions between colloidal particles, and the tendency of agglomeration is utilized as an indirect calculation of a particle's surface charge density while it is in an electrolyte solution.

2.7.8 Thermogravimetric Analysis (TGA)

TGA is a type of heating process wherein the mass of a sample is measured over time as the temperature rises. This measurement offers physical processes such as phase transitions, absorption, adsorption, desorption, and chemical phenomena such as chemisorption, thermal breakdown, and solid-gas reactions. While the temperature of a sample changes over time, the analyzer constantly measures its mass. In this technique, mass, temperature, and time are considered base measurements, from which many other values can be obtained (Coats & Redfern, 1963). In this research, the polymer-to-graphene ratio and the decomposition temperature for the inks were estimated by TGA (TA Instruments, TGA Q500, USA). The heating rate was set at 10 °C/min from room temperature to 1000 °C under air atmosphere.

2.7.9 Surface Tension

A phenomenon generated by intermolecular forces near the surface of a liquid is called surface tension. It is the level of force required per unit area to spread the surface of a liquid to occupy

the least available surface area. Surface tension is a major contributor to capillary action. The surface tension was recorded by a dynamic tensiometer (Dataphysics, DCAT11, Germany).

2.7.10 Viscosity

Viscosity is described as a fluid's resistance to progressive deformation caused by shear or tensile stress. It is another type of bulk property defined as a liquid's resistance to flow and depicts the internal friction of a flowing fluid. It can be measured as the ratio of shearing stress to velocity gradient in a fluid. The viscosity measurements of the bio-inks were measured using a viscometer (A&D, SV-10, Japan).

2.7.11 Contact Angle

The contact angle measures a liquid's ability to moisten the surface of a solid. The pattern that a drop forms on a surface is determined by the fluid's surface tension and surface composition. Surface tension creates a curved shape at the interface between droplets and the gaseous environment. Complete wetting is present at a contact angle of 0° if the liquid flows evenly on the solid surface. The surface is hydrophilic if the angle is between 0° and 90° . A non-wettable surface has an angle between 90° and 180° , and it is called hydrophobic.

The surface wettability was assessed by measuring the contact angle using a simple projector-digital camera system (Nežerka et al., 2018), and images were analyzed using ImageJ software. The contact angle was measured for droplets of nano-pure water and graphene bio-inks deposited by micro-pipette on PET substrate.

2.7.12 4-Probe resistance measurement and Profilometry

Sheet resistance (R_s), an electrical characteristic of material thin films, (also known as surface resistance or surface resistivity) is a common electrical characteristic used to characterize thin coatings of conducting and semiconducting materials. In other words, it is an important feature

for any thin film of material through, which electrical charges are intended to pass. In this technique, A current is delivered via the outer probes, causing a voltage to be produced in the inner probes.

Surface roughness, often known as roughness, is a component of surface texture. It is measured by the deviations of an actual surface from its ideal shape in the direction of the normal vector. Roughness is crucial in defining how an actual material will interact with its surroundings. in order to assess materials' roughness, the profilometry technique is used to evaluate a surface's profile.

The electrical conductivity (σ) is a fundamental property of a material that measures how well a material conducts electricity. σ of the printed graphene films were calculated from the reciprocal of R_s and thickness (t) (Equation 2).

$$\sigma = \frac{1}{R_s * t} \quad (2.2)$$

The printed films' R_s were measured by 4-point probe resistance measurements (Lucas labs 302, Canada). The films' thickness was measured by profilometry (Bruker Dektakxt, USA). All the measurements were performed at room temperature.

2.8 Conclusion

In this section, an attempt has been made to use the available facilities to perform the maximum possible analysis and studies on the ink samples and sensors made to obtain the most understanding of the work done. The discussion of the results of these studies is depicted in the chapter 3. Next, recommendations are suggested section of the future work to improve and optimize this product.

CHAPITRE 3

GREEN GRAPHENE INKS

Aqueous inks are mostly prepared from graphene derivatives such as graphene oxide (GO) and reduced graphene oxide (rGO) due to the close match between their surface energy and the surface tension of water ($72.7 \text{ mJ}\cdot\text{m}^{-2}$) (Carl L. Yaws, 2008; Shin et al., 2011; The Chemical Rubber Company, 1969). While pristine graphene and GO have a surface energy of $46.7 \text{ mJ}\cdot\text{m}^{-2}$ and $62.1 \text{ mJ}\cdot\text{m}^{-2}$, respectively (Wang et al., 2009). rGO can have surface energy between pristine graphene and GO depending on the reduction degree that affects the abundance of remaining oxygen functional groups in the graphene structure. However, GO and rGO materials possess poor sp^2 structure due to the destruction of graphene structure throughout the oxidation/reduction process. As result, they suffer of poor electrical conductivity. Here, graphene flakes are exfoliated directly from raw graphite, which maintain the sp^2 structure unaltered, expecting to preserve the optimum electrical properties for the formulated inks.

3.1.1 Biocompatible dispersants

In this study, graphene inks were comprised of water, the greenest solvent on the earth, as a continuous phase for inks' formulation. water has HSPs ($\delta_D = 15.6$, $\delta_P = 16.0$, $\delta_H = 42.3 \text{ MPa}^{1/2}$) (Barton, 1983) and surface tension ($72.7 \text{ mJ}\cdot\text{m}^{-2}$) (Carl L. Yaws, 2008; Shin et al., 2011; The Chemical Rubber Company, 1969), which are very different from those of graphene. Thus, graphene can be exfoliated only if surface-active additives (i.e. dispersants) are added to balance the surface energy between graphene and the solvent (Y. T. Liang & Hersam, 2010). To address this issue, biocompatible dispersants (gelatin, triton X-100 and tween-20) were employed to stabilize graphene in the aqueous solution. These dispersants have amphiphilic nature; (M. Johnson, 2013; Giovanni Landi et al., 2014) constituted of hydrophilic (polar) and hydrophobic (non-polar) parts. Thus, a stable dispersion of graphene can be obtained upon adsorption of the non-polar part in dispersants on graphene's surface. (G. Chen et al., 2014) While the polar part remains free in the aqueous medium, forming a hairy layer surrounding graphene layers responsible for static stabilization.

Gelatin is an attractive dispersant that has been widely used in biomedical applications because of its high viscosity, density, excellent biocompatibility, and tunable properties (Satapathy et al., 2017),(Sarvari et al., 2017). It is also a proton-conducting polymer electrolyte, making it a promising candidate for producing biodegradable energy storages based on graphene derivatives (G Landi et al., 2017), (Giovanni Landi et al., 2014), (Giovanni Landi et al., 2018), (Giovanni Landi, Sorrentino, Fedi, et al., 2015), (Giovanni Landi, Sorrentino, Iannace, et al., 2015). Alternatively, the non-ionic surfactant triton x-100 was used as a co-additive in several graphene inks to reduce surface tension (McManus et al., 2017). As a result, it can improve the printability of ink. It was also discovered to effectively avoid disrupting the electrostatic stabilization of graphene flake (McManus et al., 2017).

3.1.2 Dispersant's ratio

The polymer-to-graphene ratio and the surface coverage of graphene flakes by dispersants are key factors to control graphene's stability and concentration in dispersions.(A. Al Shboul et al., 2017; A. M. Al Shboul et al., 2018) They also directly impact the final electrical performance for the printed graphene films.(A. Al Shboul et al., 2017; A. M. Al Shboul et al., 2018) Therefore, optimizing the dispersant content is an obligation. Starting with 0.5 mg.mL^{-1} of graphite concentration in 10 mL nano-pure water, the concentration of the exfoliated graphene was recorded from the optical absorption at 660 nm. Figure 3.1 shows that by raising the dispersant concentration for triton x-100 and tween-20 from 0.1 mg.mL^{-1} to 1 mg.mL^{-1} and 1.5 mg.mL^{-1} , respectively, the quantity of the collected graphene increased from $\sim 8 \text{ mg.mL}^{-1}$ to reach the maximum of $\sim 0.11 \text{ mg.mL}^{-1}$. This indicates the successful exfoliation for $\sim 20\%$ of the initial graphite quantity, while the rest (80%) remained un-exfoliated at the bottom of the dispersion. Noteworthy, 1 mg.mL^{-1} of triton x-100 was required to reach the maximum for graphene concentration. While, tween-20 required 50% extra (1.5 mg.mL^{-1}) than triton x-100 to reach the same graphene concentration. This can indicate the superiority and feasibility of triton x-100 to adsorb on graphene's surface than tween-20. Further increase on triton and tween concentration than 1 mg.mL^{-1} and 1.5 mg.mL^{-1} , respectively, graphene's concentration decreases gradually corresponded to a depletion flocculation mechanism.(A. Al Shboul et al.,

2017; A. M. Al Shboul et al., 2018) Interestingly, the rise in gelatin's concentration from 0.1 mg.mL⁻¹ to 5 mg.mL⁻¹ has no obvious effect of increasing graphene's concentration than 0.05 mg.mL⁻¹ (2.2 folds less than dispersion with triton and tween). Accordingly, the optimal dispersants' concentrations of 0.1 mg.mL⁻¹, 1 mg.mL⁻¹ and 1.5 mg.mL⁻¹ for gelatin, triton and tween, respectively, were employed to prepare graphene inks, indicated as GGe, GTr and GTw, respectively.

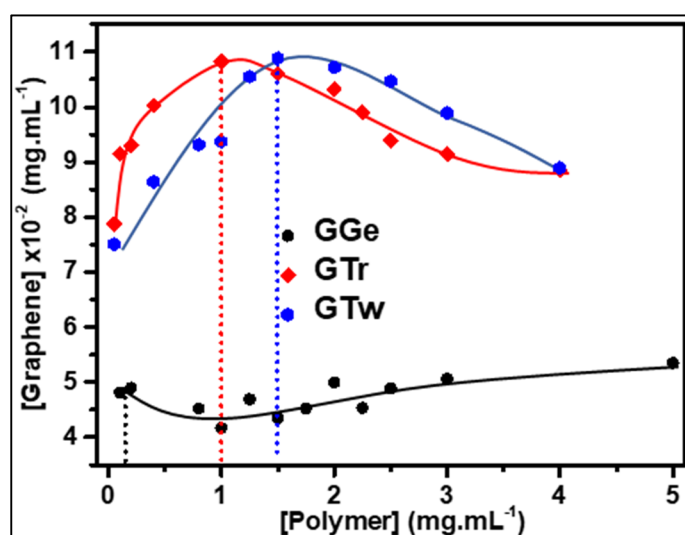


Figure 3.1 Graphene concentration as a function of dispersants' concentration

3.1.3 Zeta Potentials

To confirm the colloidal stability for graphene inks, zeta-potential was used. Typically, graphene in aqueous solutions is negatively charged, developing at the interface, which creates a potential and electric double-layer (D. W. Johnson et al., 2015). The potential is defined as the zeta-potential, which correlates strongly to dispersion stability. High magnitude zeta potentials can indicate stable dispersions due to electrostatic repulsion between particles. At pH of ~6.4, the zeta-potential was measured -38.5 mV for both GTr and GTw, while it was found -41.5 mV for GGe. This is satisfactory for highly stable dispersions to prevent the

precipitation of the graphene flakes. Based on the visual investigation and the zeta-potential measurements, graphene inks have displayed good colloidal stability for months.

3.1.4 DLS and TGA

To optimize inks' preparation toward better engineering the inks' properties, the effect of dispersants' nature and purification steps (centrifugation at 1k and 12k rpm) were investigated by DLS and TGA techniques. Knowing that inks' polymer content and the surface coverage of graphene flakes by polymers are crucial parameters required to consider adjusting charge transfer in graphene films (A. Al Shboul et al., 2017), and flake size distribution (Martínez-Flores et al., 2019).

3.1.5 DLS

DLS is a typical technique to measure particle size distribution smaller than 5 μm . However, it has been exploited as a large-scale estimation of the mean flake size for graphene flakes in graphene dispersion. Flake size is an important characteristic to consider avoiding clog the printing nozzle; a complication can occur during the printing process.

DLS determined the flake size distribution of the inks as a function of the purification steps. After centrifugation at 1k rpm for 30 minutes (the first purification step), graphene dispersions have a diameter distribution range of 50 nm - 800 nm (Figure 3.2A) with > 90% of flakes in the range of 50 nm - 600 nm, in agreement with the flake size produced by LPE technique (Backes et al., 2016). While the peak maxima in the DLS curve distributions for GTr and GGe based are centered at 300-500 nm. The DLS curve distribution for GTw is centered at 200-400 nm. By analyzing the area under the curve, GTr and GGe dispersions comprised of 46.2% and 48%, respectively, flakes smaller than 400 nm (<400 nm). The GTw is composed of 67.8% of flakes <400 nm indicating a 20% smaller flakes than GTr and GGe dispersions. Flakes larger than 400 nm (> 400 nm) occupied 52%, 53.8% and 32.2% for GGe, GTr and GTw, respectively.

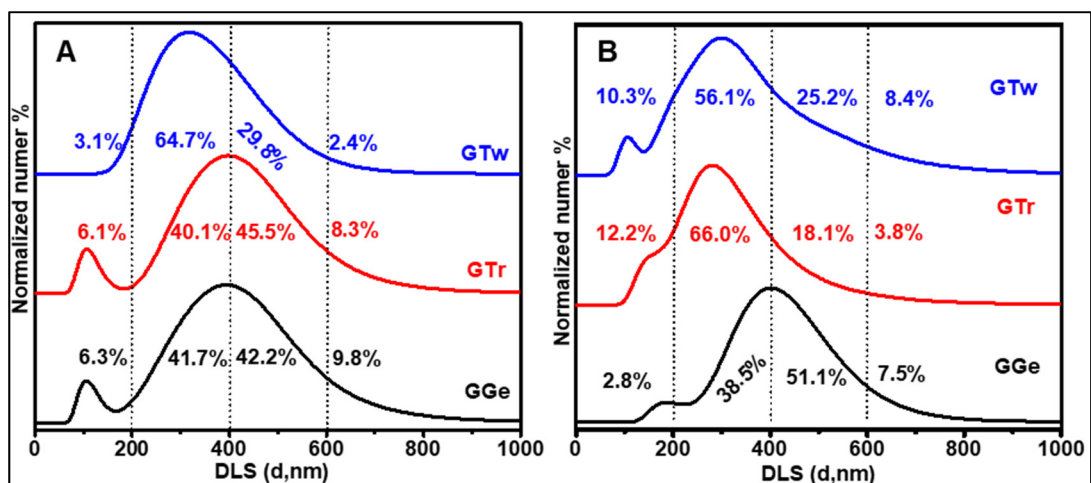


Figure 3.2 DLS analysis of the diameter distribution for graphene dispersion prepared with gelatin, triton, and tween dispersants

The flake size distribution of the final inks after collecting graphene from the second purification process (centrifugation at 14k rpm for 2 hours), DLS analysis shows a shrinking for the diameter distribution range to 100 nm - 800 nm as well as the flakes' distribution, as shown in Table 3.1 and Figure 3.2B. While the DLS curve for GTr and GTw are centered at 200-400 nm. The DLS curve for GGe is centered at a larger range of 300-500 nm. Moreover, GTr and GTw dispersions showed an elevation to 72.2% and 66.4%, respectively, for flakes smaller than 400 nm (< 400 nm). The GGe showed a shrinking from 48% to 41.3% of flakes < 400 nm, indicating a >25% less small flakes than GTr and GTw. Flakes larger than 400 nm (> 400 nm) occupied 58.6%, 21.9% and 33.6% for GGe, GTr and GTw, respectively, showing a significant reduction for the large flakes in GTr than ones for GTw and GGe. It thus appears that GTr has the smallest flakes, followed by GTw and GGe, respectively. Hypothetically, the small flakes' importance was raised because they can play a key role as nanofillers in the printed films. Therefore, they can enhance the charge transport throughout the graphene films resulting from increasing their electrical conductivity. Besides, the DLS analysis shows the possibility to drive flake size distribution by dispersants' nature.

Table 3.1 Graphene Flake size distribution as a function of the dispersant and purification process. Whereas the first purification step was performed by centrifugation at 1k rpm for 30 minutes. The second purification step was performed by centrifugation at 14k for 2 hours

Graphene Flake size distribution						
	GGe		GTr		GTw	
d (nm)	1k rpm	1k + 14k rpm	1k rpm	1k + 14k rpm	1k rpm	1k + 14k rpm
<200	6.3	2.8 (-55.6%)	6.1	12.2 (+50%)	3.1	10.3 (+69.9%)
200-400	41.7	38.5 (-7.7%)	40.1	66.0 (+39.2%)	64.7	56.1 (-13.3%)
400-600	42.2	51.1 (+17.1%)	45.5	18.1 (-60.2%)	29.8	25.2 (-15.4%)
>600	9.8	7.5 (-23.5%)	8.3	3.8 (-54.2%)	2.4	8.4 (+71.4%)

3.1.6 TGA

For evaluation polymer-to-graphene ratio and graphene's thermal stability, TGA analysis was also conducted as a function of the purification processes. As observed in Figure 3.3C, raw Gt (7-10 μm) decomposed in the range of 550-850 $^{\circ}\text{C}$ that deconvolute to a prominent peak at 780 $^{\circ}\text{C}$ and a shoulder at 620 $^{\circ}\text{C}$ (Figure 3.3D). Upon 1k rpm centrifugation process (Figure 3.3A), The collected graphene flakes showed a decomposition range of 500- 750 $^{\circ}\text{C}$ for GTr and GTw, while GGe exhibits much higher thermal stability in the range 500-780 $^{\circ}\text{C}$. Corresponding to the variation on the initial polymer content used during the inks' preparation, dispersants are estimated in the derivative thermograms (DTG) as 14% for gelatin (250-580 $^{\circ}\text{C}$) in GGe, 19% for triton (200-400 $^{\circ}\text{C}$) in GTr, and 26% for tween (200-450 $^{\circ}\text{C}$) in GTw.

Upon employing the 14k rpm step, the final inks (Figure 3.3D) showed a significant reduction in the polymer content for triton and tween to reach 7% and 5% in GTr and GTw, respectively. It thus appears that the removed triton and tween dispersants mainly were bonded to the small

graphene flakes, which were removed with their supernatants by the 14k rpm centrifugation process. Additionally, graphene's thermograms in the range 500-780 °C for GTr and GTw were shrunk to semi-symmetrical peaks at 680 °C and 690 °C, respectively, correlated with the small flakes' removal indicating the flake size effect on flakes' thermal decomposition. The DTG curve for GGe shows a slight reduction in the gelatin content to 13% (Figure 3.3B). It thus indicates the successful removal of the excess gelatin dispersant upon centrifugation at 14k for 2 hours. The thermogram for GGe preserved a similar DTG (Figure 3.3D) corresponded to the minor change on the flake size distribution, as was found by DLS analysis.

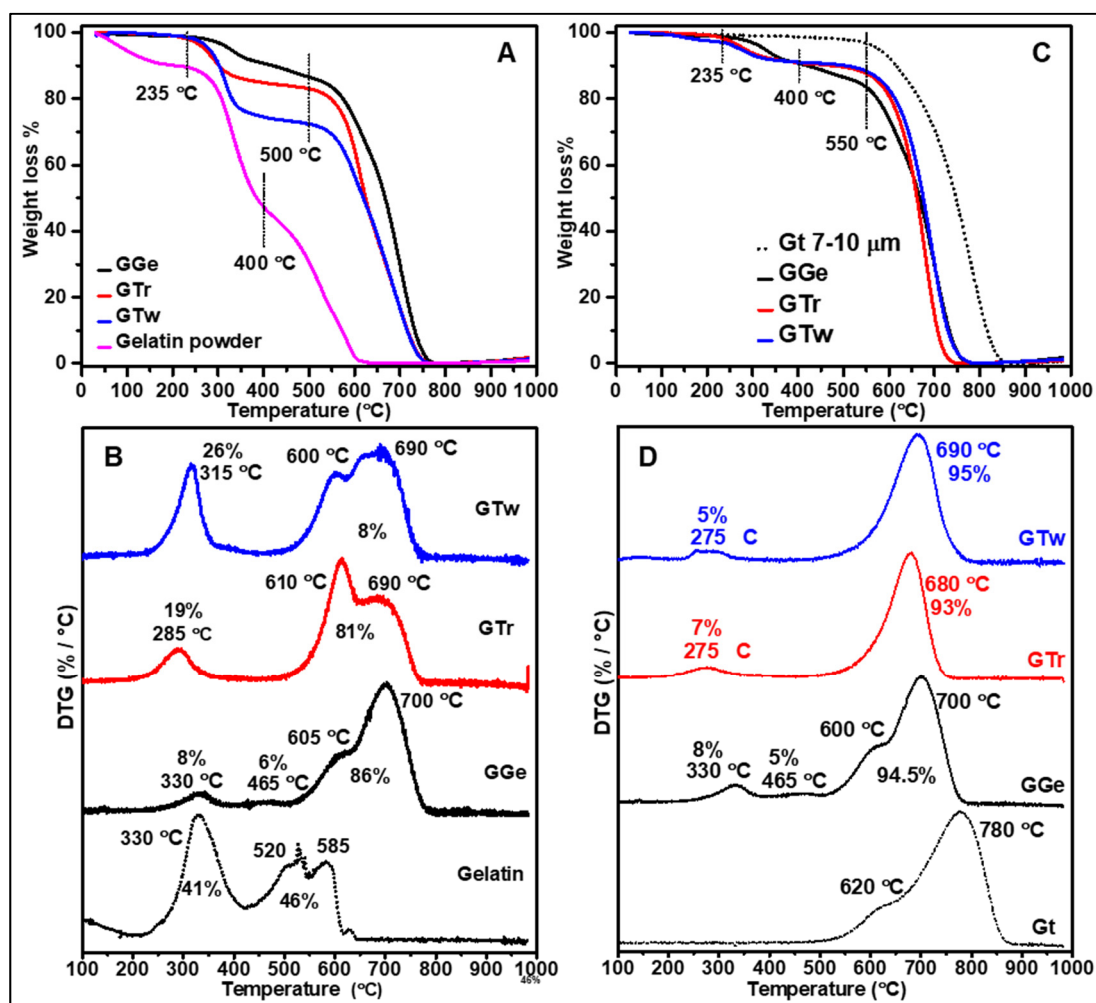


Figure 3.3 Thermograms of TGA and derivative (DTG) of raw Gt, gelatin, GGe, GTr and GTw as a function of the dispersant and purification process. (A,B) the gelatin and graphene samples after the centrifugation at 1k rpm for 30 minutes. (C,D) Raw graphite and graphene inks after centrifugation at 14k rpm for 2 hours

3.1.7 AFM and TEM

The morphological characteristics of graphene inks can be observed in AFM (Figure 3.4) and TEM (Figure 3.5) images. AFM demonstrates a similar dimension distribution of the exfoliated nanosheets in the three graphene inks (GTr, GTw and GGe) ranging from 50 nm to 500, which agrees with the major flake distribution found in DLS. The determined thickness of the exfoliated nanosheets evaluated from the surface profile was ranged from 1 nm to 4 nm, indicating few-layer graphene flakes were produced in the aqueous inks via the LPE. However, the coating of the adsorbed stabilizers-like residue on the graphene surface is another observation consistently revealed in the AFM images that are roughly estimated from the surface profile in the range of 1 nm to 4 nm. These coatings complicate the accurate estimation of the number of graphene layers by measuring the thickness of the exfoliated graphene nanosheets. By measuring the surface roughness of graphene sheets from GGe (13 wt% gelatin as measured by TGA), the accumulations of the adsorbed stabilizers showed a thickness that can reach 10 nm of height. While graphene nanosheets found in GTr and GTw showed smaller accumulations ranging from 1 nm in GTr (7 wt% triton) to 2 nm in GTw (5 wt% tween).

This was further confirmed by the TEM images, as shown in Figure 3.5. TEM images reveal similar morphologies of graphene sheets with some overlapping regions. Besides, TEM micrographs demonstrate the tendency of individual graphene flakes to re-stack as soon as the solvent dried, forming an accumulated graphene sheet. TEM images confirm the formation of mono- and few layers of graphene sheets with a length of 400-600 nm and width of 150-300 nm. The black areas distributed on the graphene layers are likely to be the piled dispersant that is adsorbed on the graphene surface, which is consistent with the observation from AFM images.

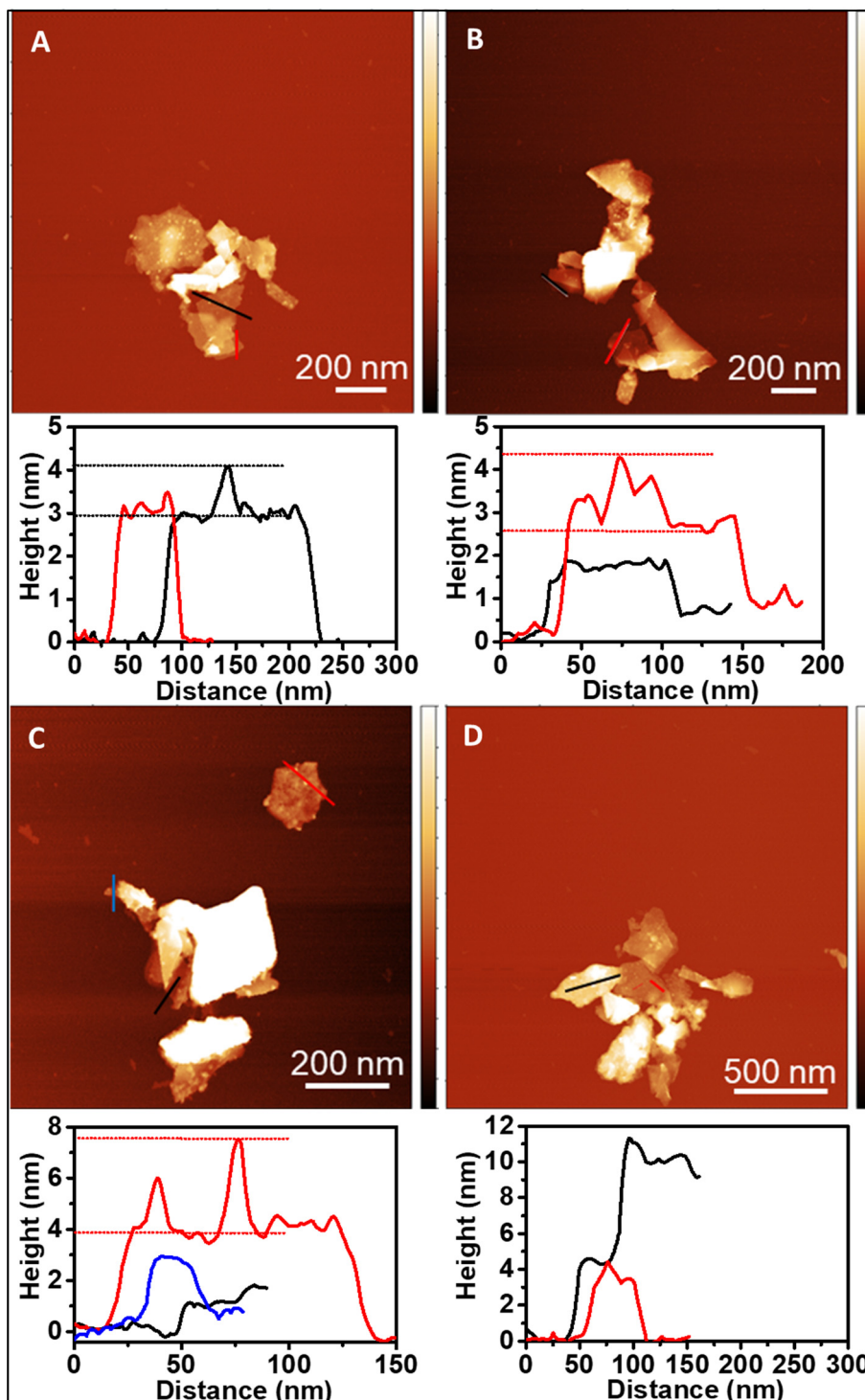


Figure 3.4 AFM images and surface profile from graphene nanosheets from (A) GTr, (B) GTw, and (C,D) GGe. The surface profiles highlight the variation in thickness related to the coating of the adsorbed stabilizers-like residue on the graphene surface

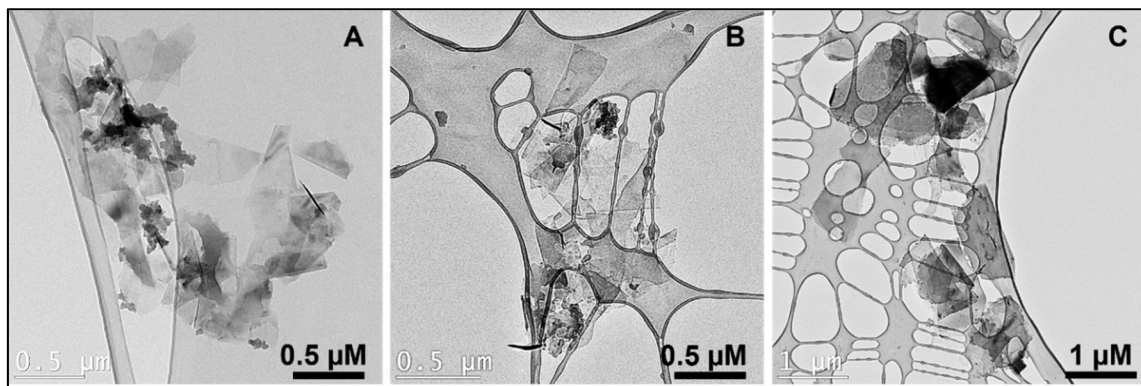


Figure 3.5 TEM images of graphene sheets from (A) GTr, (B) GTw, and (C) GGe inks

3.1.8 Electrical Properties

To study the electrical behavior of the graphene inks as a function of thickness (t), the graphene inks were translated into thin films placed on the plastic substrate PET for a given number of printing passes using an AJP, as shown in the digital image in Figure 3.6A-C. Simply without any other additions to control inks' properties (viscosity, surface tension, printing flow, rheology modifier..etc), inks can readily flow through the nozzle during printing. The acquired inks have a good dispersity with minor signs of precipitation even if stored for more than a month. Considering the two main aspects of performance, the graphene inks should afford good printability and high printing definition. These inks are satisfactory promising.

3.1.9 4-Probe measurements and Profilometry

The electrical characteristics of graphene inks are determined using a four-point probe measurement of sheet resistance, while the film thickness is determined using profilometry. The thickness of the films began at 85 nm for printing one layer on PET substrate and increased by 32 nm for each consecutive printed layer. As a result, the thickness reached 720 nm for 20 layers and 1.5 μm for 40 layers. As shown in Figure 3.6D, 250 nm thickness was sufficient to measure sheet resistance in between 160-170 $\text{k}\Omega/\square$ for graphene printed films, where no

electrical resistance measurement was detected for thinner films. By increasing films' thickness, the sheet resistance decreases inversely to settle at 7.5 k Ω/\square , 3.6 k Ω/\square and 2.6 k Ω/\square for GTr films at 500 nm, 800 nm and 1.15 μm film's thickness, respectively. For GTw, R_s settles to 14.4 k Ω/\square , 7 k Ω/\square and 5 k Ω/\square for 500 nm, 800 nm and 1.15 μm film's thickness, respectively, which shows almost double the R_s measured for GTr films for the same films' thickness. GGe films showed the highest sheet resistance with 27 k Ω/\square , 17 k Ω/\square and 14 k Ω/\square for 500 nm, 800 nm and 1.15 μm film's thickness, respectively. The high electrical resistance for GGe is attributed to high gelatin content (13%), resulting in hinder the charge transfer between graphene flakes, and therefore high R_s of the printed films were achieved.

For conductivity (σ) evaluated from the reciprocal of R_s and t ($\sigma = (R_s \cdot t)^{-1}$), Figure 3.6E, σ is stable for $t > 500\text{nm}$ with an average 3.5 S.cm $^{-1}$, 1.5 S.cm $^{-1}$ and 0.8 S.cm $^{-1}$ for GTr, GTw, and GGe, respectively. The conductive properties of graphene inks are still far from being a replacement for metallic inks. However, the resistance is sufficiently suitable for the fabrication of chemiresistive sensors. For the remainder, post-treatment like annealing or compression rolling can significantly decrease the sheet resistance of printed graphene by improving interlayer contacts.

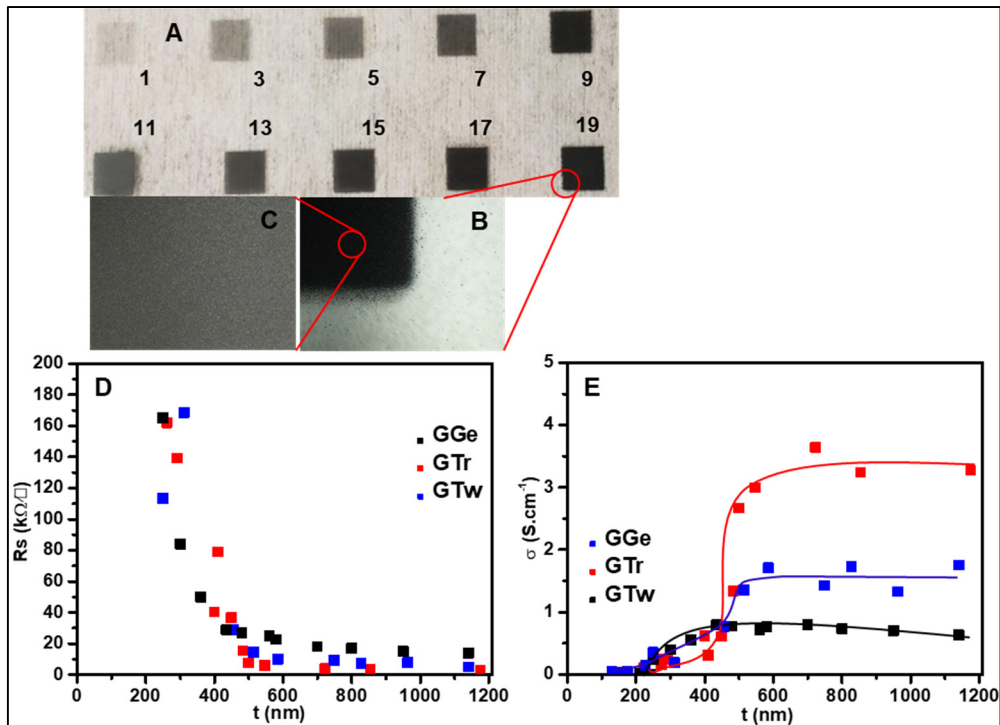


Figure 3.6 (A) Optical microscope of Aerosol-Jet printed GTr films on a PET substrate. (B,C) Optical microscope images for a graphene film's edge and center. (D) R_s and (E) σ as a function of films' thickness

3.1.10 Raman

Generally, materials' quality and interlayer contacts (interconnectivity) between flakes are key factors determining the electrical properties of printed graphene structures. Raman spectroscopy is a typical informative tool to investigate the sp^2 quality structure (or graphitization degree) as measured from the intensity ratio between D and G peaks (i.e. I_D/I_G ratio). As shown in Figure 3.7, Raman spectroscopy shows characteristic peaks for the raw graphite and the graphene inks at $\sim 1335\text{ cm}^{-1}$ (D-band), $\sim 1574\text{ cm}^{-1}$ (G-band) and $\sim 2666\text{ cm}^{-1}$ (2D band). Noteworthy, the presented spectra are the Raman spectra' median representatives taken at 10 different spots on each sample. The Raman spectrum for the raw graphite reveals an I_D/I_G ratio of 0.12, indicating a well crystallized bulk graphite feature. Graphite typically shows a I_D/I_G ratio equal to zero. However, the larger I_D/I_G ratio (0.12) observed for graphite can be attributed to performing a bulk measurement for graphite powders with a distribution of smaller flakes (Brennan et al., 2017). Upon exfoliation, the D-band slightly increases

resulting in a slight elevation on I_D/I_G ratios (0.23 – 0.28). This suggests a small increase in the disorder level of the graphene layers upon exfoliation process compared with the raw graphite. Still, the elevation on the I_D/I_G ratios is not significant to explain the variation in graphene inks' electrical properties.

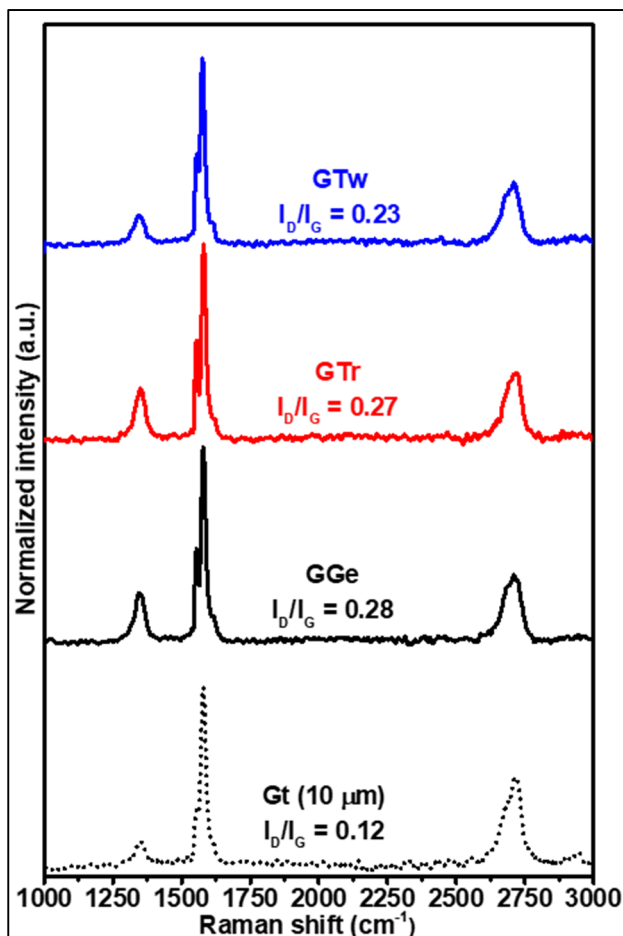


Figure 3.7 Raman spectra for printed films of the graphene bio-inks

3.1.11 Inks' Wettability and Flake's Interconnectivity: Contact Angle and SEM

Alternatively, flake's interconnectivity and inks' wettability play a key role in films' conductivity. Inks' wettability is an important parameter that controls the interaction between substrate and graphene inks, which depends on the match between inks' surface tension and

the surface energy for PET substrate (Torrise et al., 2012). Good wettability influences inks' printing quality and films' smoothness (C.-Y. Xu et al., 2017), affecting films' electrical performance. The contact angle was measured by dispensing a drop of graphene ink on the PET substrate to evaluate wettability. The better wettability is measured with the smaller the contact angle obtained. Figure 3.8 shows the droplet shape just after it lands on the PET substrate. The contact angle measurements for the graphene inks indicated the smallest of 42° was achieved for GTr, demonstrating the best wetting performance over PET substrate. While GTw and GGe showed a contact angle of $\sim 55^\circ$ illustrating a lower adhesion property.

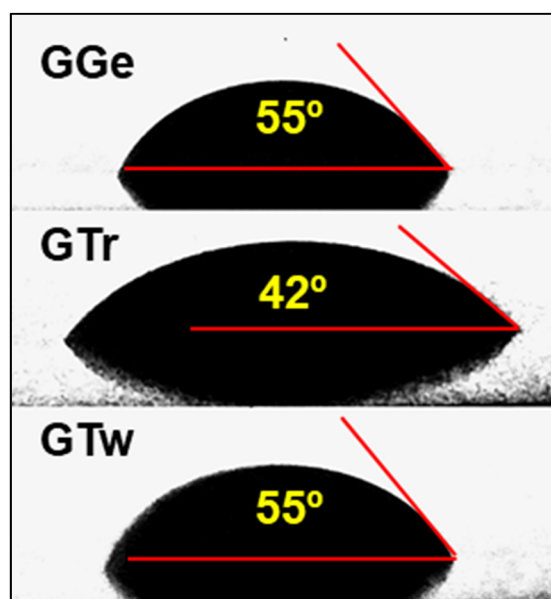


Figure 3.8 Contact angle measurements for GGe, GTr and GTw over PET substrates

Graphene flake's interconnectivity works collaboratively with the genuine flakes' properties to facilitate the charge transport throughout films. SEM characterized the surface morphology of the graphene films printed on the PET substrate. Figure 3.9 shows a surface view of the graphene film screening how the stacked flakes make up the film's architecture. Figure 3.9(A,B) shows the heavily coated GGe film with white accumulations resulting in a wrinkled graphene film that can be ascribed to the high gelation content (13%). Incorporating the

nonconductive dispersants obstruct interlayer contacts, thereby rendering the charge transfer throughout the GGe film resulting in poor electrical contact between graphene flakes.

A lower degree of wrinkled film structure with less accumulation appears for GTw (Figure 3.9(E,F)). However, GTr film exhibits a densely packed film structure and smooth film (Figure 3.9(C,D)). Higher magnification images confirm the densely packed structure and smooth GTr film (Figure 3.9D), completely different from those for GTw and GGe, as shown in Figure 3.9(B,F), respectively. Well-stacked films create good contact between adjacent graphene nanosheets assuring the charge transfer and therefore augment the finished electrical conductivity. Consequently, the consistent GTr film explains the high electrical conductivity compared to GTw and GGe.

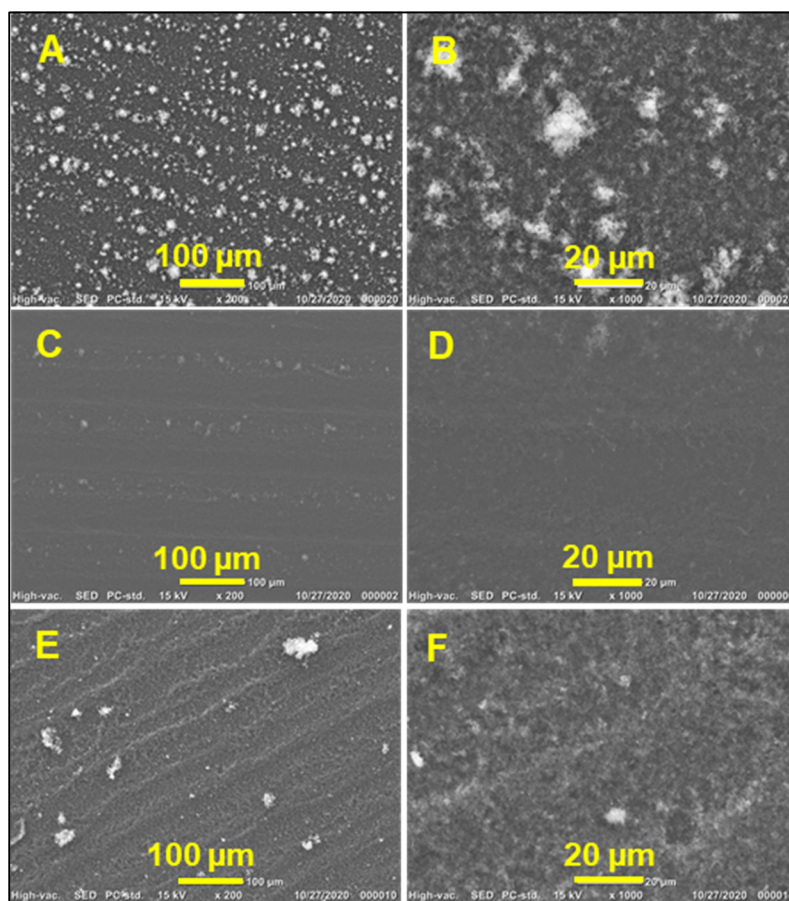


Figure 3.9 SEM images of graphene films printed from (A,B) GGe, (C,D) GTr, and (E,F) GTw

For GTr, however, the high percentage of the small graphene flakes < 200 nm (12.2%) as found in DLS analysis can benefit the electrical conductivity of graphene films compared to GTw and GGe. Small flakes can fill up the voids of the network structures. It thus enhances flake's interconnectivity as well as uniformity and density of printed films. This can be explained by the fact that they would bridge between graphene flakes offering network frame and π - π interactions with graphene flakes, thus forming additional channels for charge transport within the film. This explains the reduction in conductivity for GTw (10.3%) and GGe (2.8%) by the reduction in the amount of the small graphene flakes <200 nm. Consequently, GTr ink was employed for the rest of the research to print graphene-based chemiresistive sensors for humidity detection.

3.2 Graphene Humidity Sensors

One of the rare examples of aerosol printed graphene humidity sensors is presented in this thesis. Furthermore, because the inks employed are environmentally friendly, the resulting sensors avoid the discharge of harmful materials into the environment and help to reduce e-waste in nature. They may also be user-friendly when in contact with sensitive subjects such as human skin.

3.2.1 GTr Response

Figure 3.10 illustrates the humidity response curve for GTr sensor with the dimensions of 1 mm length x 500 μ m width x 400 nm thick with the electrical resistance of 200 k Ω in air ambient. This curve could be divided in two periodic cycles of humidity range from 30%-67% and 67%-90% at a nearly fixed temperature of 25°C. The humidity sensing performance of GTr can be divided into two stages depicted in Figure 3.10. When exposed to the moderate RH environment (30%RH–67%RH), the GTr sensor response increases from 20% to 30% responding to the water molecules' adsorption on the hydrophilic sites at the graphene surface. The weak response could be attributed to the insufficient hydrophilic sites on the graphene surface for water adsorption. At higher RH (RH > 67%), a reduction in the electrical resistance

was observed. Hypothetically, the dramatic change of electrical resistance values under high humidity ($> 67\%RH$) was primarily due to the insufficient mechanical property to maintain the integrity of the thin films' structure at high humidity levels. The poor sensing performance for GTr sensor urged to improve the mechanical properties for the ink which showed poor humidity sensing properties.

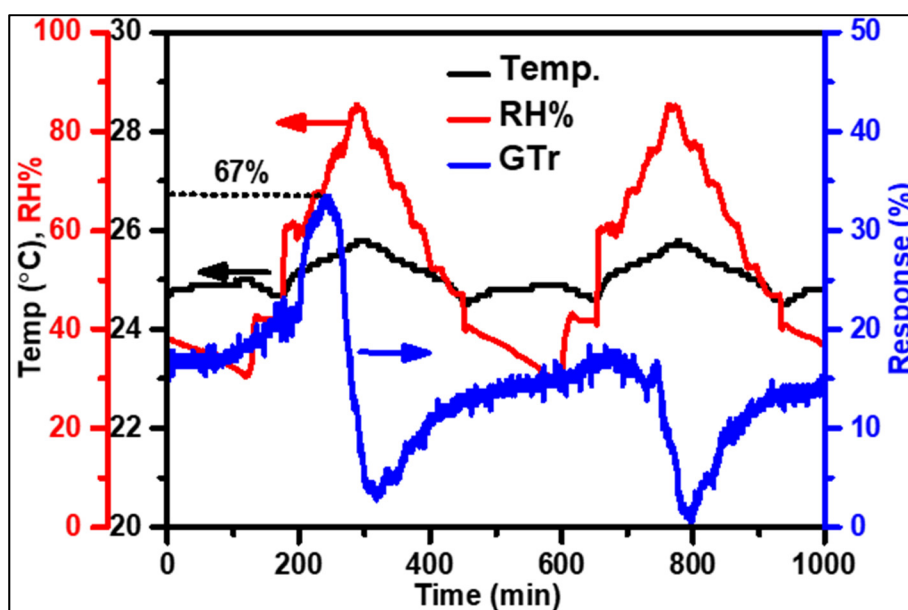


Figure 3.10 The adsorption and desorption response curves for GTr sensor

3.2.2 Ge-GTr Response

Gelatin (Ge) is a biocompatible material that was added to GTr as a binder to improve the mechanical stability of the printed films. Besides, it was beneficial as a co-sensing material for humidity detection. Figure 3.11 shows a microscope image for the 1Ge-GTr sensor. These images show that the as-fabricated sensor has a thin sensing graphene film of 400 nm thick, which guarantees H_2O molecules to penetrate through the graphene film to anchor on the active sites in the sensor's bulk.

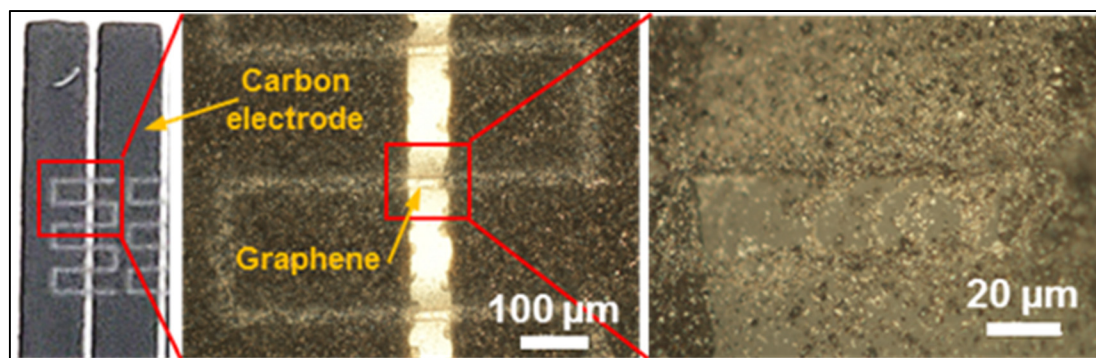


Figure 3.11 Optical microscope images of 1Ge-GTr sensors showing the flexible carbon electrodes and the printed graphene thin films

Upon modifying GTr with 0.1 mg.mL^{-1} Ge, the 0.1Ge-GTr sensor (Figure 3.12A) showed a similar sensing performance as same as the non-modified GTr sensor (Figure 3.10), which is supposed to insufficient gelatin modification. With 0.25 mg.mL^{-1} gelatin modification, the 0.25Ge-GTr sensors showed an improved humidity detection with an inversed electrical behavior. While GTr and 0.1Ge-GTr showed a decrease in the response at high humidity levels. The 0.25 Ge-GTr showed an increase in the response with the humidity increase and vice versa.

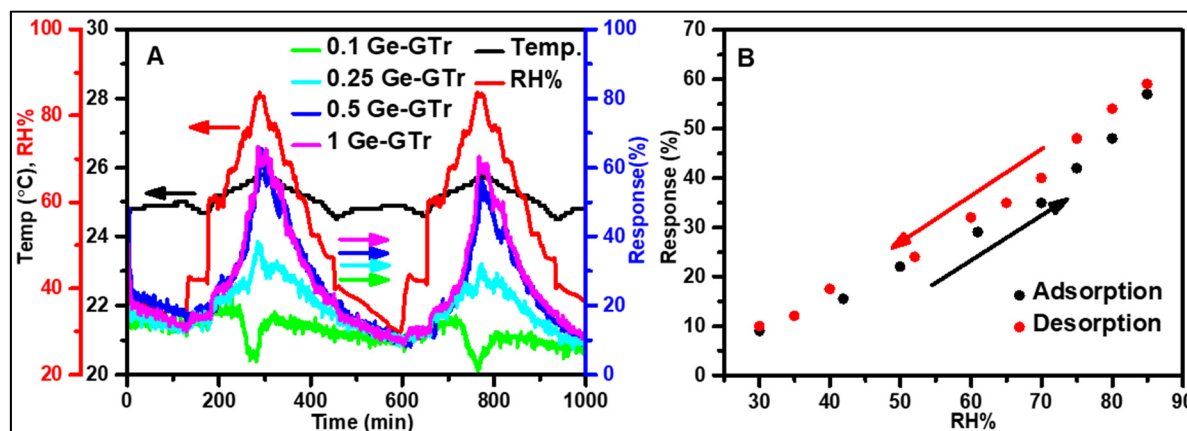


Figure 3.12 (A) The adsorption and desorption response curves for Ge-modified GTr sensors. (B) The Summary for adsorption and desorption responses versus humidity for the 1Ge-GTr on the surfaces

As observed from the adsorption and desorption response curves on figure 3.12B, the Ge-modified GTr sensors with gelatin concentration from 0.5 mg.mL^{-1} and 1 mg.mL^{-1} showed a drastic improvement in the humidity sensing performance. Compared to unmodified and low gelatin-modified sensors, the abundance of the hydrophilic sites guaranteed better humidity sensing performances. Besides, they showed good repeatability and stability in two periodic cycles of humidity. Therefore, they were selected to further study the humidity sensing properties for the rest of the work. The RH response analysis when measuring and describing humidity for the 1Ge-GTr sensor is plotted in Figure 3.12B. The 1Ge-GTr sensor showed a good linear response from 10% to 60%, when humidity increased from 30% to 90% investigated at a constant temperature of 25°C . Besides, they exhibited a sensitivity of $0.55\%/RH\%$ with negligible hysteresis and ultrafast response in a second.

The humidity sensing mechanism of nonmodified and low gelatin-modified sensors could be explained as follows. The adsorbed H_2O molecules serve as electron-withdrawing molecules (acceptors), inducing electrons to be transferred from the graphene surface. This increment of hole concentration leads to reduced electrical resistance [37]–[40]. For higher gelatin-content sensors (0.25 , 0.5 , and 1 mg.mL^{-1}), an increase in the electrical resistance was observed by contributing to the swollen gelatin binder surrounding graphene flakes. As humidity level increases, more H_2O molecules attach to the surface, leading to a more significant separation between graphene flakes. As a result, a reduction of the charge transfer through the conductive graphene film which increases the electrical resistance for sensors.

3.2.3 Response and Recovery Time

Figure 3.13 Depicts exemplary response and recovery time data for the 1 Ge-GTr thin sensing film. RH values for these measurements were obtained from the resistive sensor response curves using the environmental RH chamber at ETS. Figure 3.13 (A) illustrates that when the data logger's recorded humidity increases from 50% RH to 70% RH in 80 seconds, the 1 Ge-GTr sensor signal increases concurrently and exhibits the same performance of 1 RH%

increase every 4 seconds. Figure 3.13 (B) shows the recovery period as humidity decreases from 75% RH to 40% RH. The 1 Ge-GTr sensor is performing again similarly to the data logger in terms of sensor sensitivity. Despite the fact that the recovery time is nearly 80 seconds for each 1 RH% decrease, which is substantially longer than the response time, this issue was caused by a defective environmental chamber that was unable to remove humidity faster.

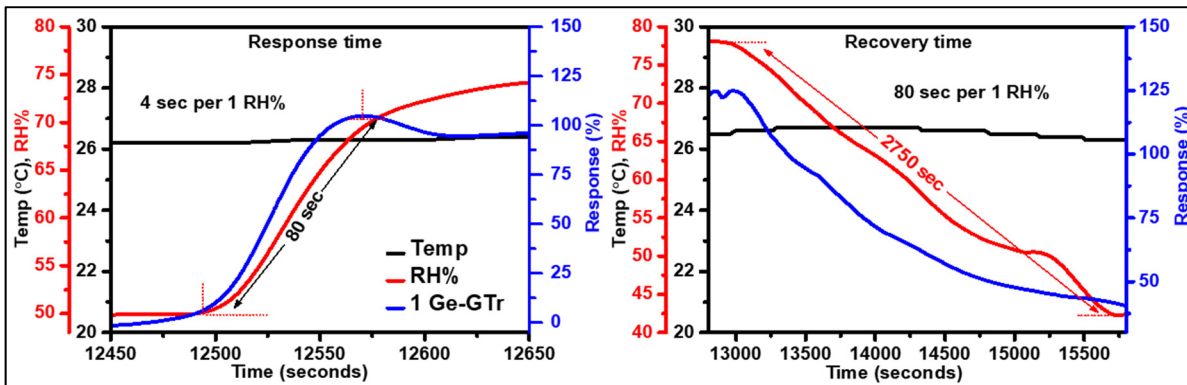


Figure 3.13 (A) Response and (B) recovery time curve of 1 Ge-GTr based sensor to humidity at working temperature of 25°C

3.2.4 Temperature Effect

Figure 3.14 shows the temperature response for the 1Ge-GTr sensor in a range of 22°C - 70°C. Although the humidity was maintained at RH \approx 30% to exclude the humidity effect on the sensor's response curve, a reduction was observed in humidity with temperature elevation from 30°C to 70°C. The 1Ge-GTr sensor showed minimal response to the temperature variation. The observed reduction of the electrical resistance could be attributed to the humidity reduction to RH \sim 10% at a temperature of 70°C. As a result, the 1Ge-GTr sensor possesses a good sensitivity to humidity, fast response, good stability and repeatability, and good inertness to temperature fluctuation. These results imply significant advantages for IoT applications.

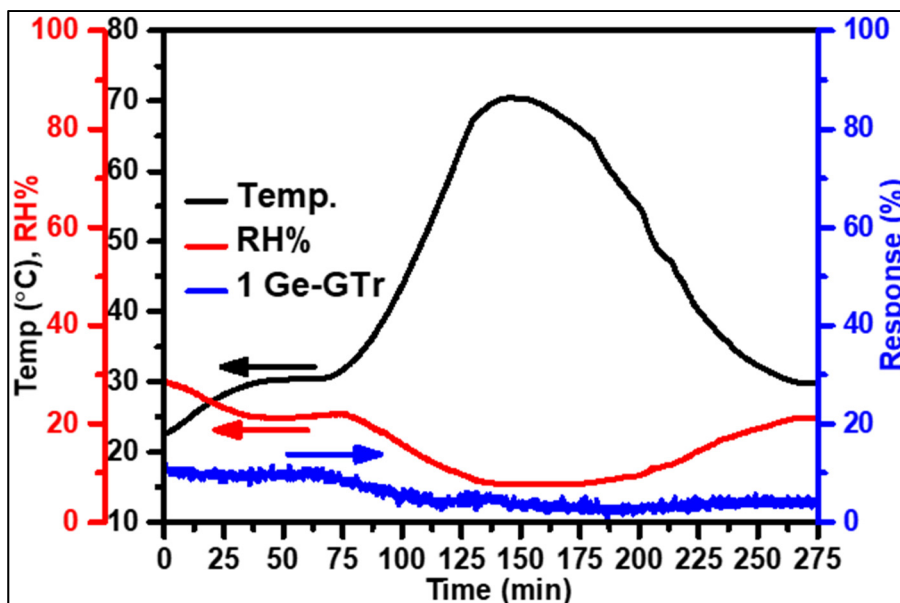


Figure 3.14 The response curve to temperature for the 1Ge-GTr sensor

3.3 Discussion

In this study, we first succeeded in the preparation of colloiddally stable pristine graphene in water using biocompatible dispersants (gelatin, triton X-100 and tween 20). 0.1 mg/mL of gelatin, 1 mg/mL of triton and 1.5 mg/mL of tween were found to effectively formulate green graphene inks. Whereas LPE of pristine graphene assisted to avoid alteration the properties of graphene flakes. The use of environmentally-friendly materials facilitated extension the practical applications of the green graphene inks in application when they get in contact to vital subjects such as human skin. As a function of the dispersant type used through the inks' preparation, the final graphene inks showed a variation mainly in the flake size distribution as well as wettability and surface smoothness of printed films on top PET substrates. Consequently, the optimum electrical conductivity (3.5 S.cm^{-1}) was achieved for GTr, owing to high content of small graphene flakes ($< 200 \text{ nm}$), better wettability and better flakes interconnectivity in the printed films. The investigations on the GTr ink proposes the potential application of the GTr as conductive green graphene ink to fabricate printed and flexible green chemo-resistive sensors.

Later, chemo-resistive humidity sensors were fabricated based on printed electronic technology with graphing inks dispersed in water. From the investigated results and analysis, it is obvious that both series of sensors made of graphene-triton ink (GTr) and gelatin-graphene-triton ink (Ge-GTr) were sensitive to humidity change. The sensors made of GTr presented a linear response up to 67% of RH. above that level, they showed dramatic failure, which could be explained by the dissociation that happened between graphene flakes inside the sensing layer due to a high concentration of H₂O molecules. On the other side, sensors made of Ge-GTr illustrated much better response due to presence of gelatin molecules in the ink combination which enhanced the unity of the printed sensing film.

While 0.1 Ge-GTr sensors showed similar responses as GTr sensors. 0.25 Ge-GTr sensors showed a good response to humidity, but the response magnitude was not high enough. The best results came from 0.5 and 1 mg/ml sensors. They presented a good linear response that is directly proportional to humidity changes from 30% to 90% RH as same as the commercial data logger (OMEGA) graphed which was discussed previously in results section. On the other hand, these sensors showed a high stability to temperature ranging from 22 °C to 70 °C with a small variation which could be negligible.

CONCLUSION

This work presents the preparation of GGe, GTr, and GTw; aqueous and environmentally friendly graphene inks assisted by biopolymers; gelatin, triton X-100, and tween-20, respectively. By employing water as a solvent and biocompatible dispersant, these inks are indicated as green inks that can assist in avoiding releasing harmful material to the environment upon degradation. The inks were conductive ($R_s = 2.4 - 14 \text{ k}\Omega/\square$) and were easily printed on PET using an AJP. In contrast, the biopolymers have no evident influence on graphene's quality (I_D/I_G ratios $\approx 0.23 - 0.28$). They played a critical role in the flake diameters distribution and inks' adhesive properties, resulting in a smooth and uniform surface for GTr films. This suggests excellent interconnectivity between graphene flakes for GTr. Therefore, a better electrical conductivity of $3.5 \text{ S}\cdot\text{cm}^{-1}$ was achieved.

Flexible aerosol-jet printed graphene-based sensors were fabricated using pure and gelatin-modified green graphene inks. Sensors showed an enhanced humidity sensitivity with the gelatin modification due to the increase in the hydrophilic sites that act as adsorption sites for H_2O molecules. Therefore, (0.5 and 1) Ge-GTr sensors possess superior response and better linearity than nonmodified and low content modified (0.1 and 0.25) Ge-GTr sensors. The 1Ge-GTr sensor successfully demonstrated linear response to humidity variation in the range of 30% - 90%, while not showing interference to a temperature change in a range between 22 – 70 °C. The 1Ge-GTr sensor also demonstrated a good sensitivity of 0.55/%RH at 25°C. The results indicate that the sensors' electrical resistance change depends on the degree of graphene's surface coverage with gelatin upon humidity detection.

FUTURE WORK

Bridge Sensor

Comparing regular sensor, which has one surface exposing the environment, bridged sensors can be advantageous to increase the surface area for sensors as they have two surfaces to expose to humidity. This means that somehow more surface for detection and also faster and more precise response. In the first attempt, a photoresist (SU82002) was printed in the gap between silver electrodes the electrode spacing is 200 μm . Then the sensing layer of graphene is printed on top of the photoresist. The graphene pattern is 3 mm ladder pattern 10 steps, and the width of graphene layer is 40 to 50 μm . Finally, the photoresist will be removed by acetone. During preliminary tests, while photoresist was removed by acetone, part of the graphene bridge remained, and other parts collapsed. From our point of view, these elementary results are promising to continue investigating in the future the humidity sensors based on graphene bridges.

LIST OF BIBLIOGRAPHICAL REFERENCES

- Ahn, H. Y., Kim, J.-G., & Gong, M.-S. (2012). Preparation of flexible resistive humidity sensors with different electrode gaps by screen printing and their humidity-sensing properties. *Macromolecular Research*, *20*(2), 174–180. <https://doi.org/10.1007/s13233-012-0085-3>
- Al Shboul, A. M., Siaj, M., & Claverie, J. P. (2018). Selective Process To Extract High-Quality Reduced Graphene Oxide Leaflets. *ACS Applied Nano Materials*, *1*(10), 5920–5926. <https://doi.org/10.1021/acsnm.8b01580>
- Al Shboul, A., Trudeau, C., Cloutier, S., Siaj, M., & Claverie, J. P. (2017). Graphene dispersions in alkanes: toward fast drying conducting inks. *Nanoscale*, *9*(28), 9893–9901. <https://doi.org/10.1039/C7NR01919J>
- Ali, S., Hassan, A., Hassan, G., Bae, J., & Lee, C. H. (2016). All-printed humidity sensor based on graphene/methyl-red composite with high sensitivity. *Carbon*, *105*, 23–32. <https://doi.org/10.1016/j.carbon.2016.04.013>
- Andrić, S., Tomašević-Ilić, T., Bošković, M. V., Sarajlić, M., Vasiljević-Radović, D., Smiljanić, M. M., & Spasenović, M. (2021). Ultrafast humidity sensor based on liquid phase exfoliated graphene. *Nanotechnology*, *32*(2). <https://doi.org/10.1088/1361-6528/abb973>
- Arapov, K., Abbel, R., De With, G., & Friedrich, H. (2014). Inkjet printing of graphene. *Faraday Discussions*, *173*, 323–336. <https://doi.org/10.1039/c4fd00067f>
- Ates, T., Tatar, C., & Yakuphanoglu, F. (2013). Preparation of semiconductor ZnO powders by sol-gel method: Humidity sensors. *Sensors and Actuators, A: Physical*, *190*(January), 153–160. <https://doi.org/10.1016/j.sna.2012.11.031>
- Aziz, S., Chang, D. E., Doh, Y. H., Kang, C. U., & Choi, K. H. (2015). Humidity Sensor Based on PEDOT:PSS and Zinc Stannate Nano-composite. *Journal of Electronic Materials*, *44*(10), 3992–3999. <https://doi.org/10.1007/s11664-015-3914-2>
- Backes, C., Szydłowska, B. M., Harvey, A., Yuan, S., Vega-Mayoral, V., Davies, B. R., Zhao, P., Hanlon, D., Santos, E. J. G., Katsnelson, M. I., Blau, W. J., Gadermaier, C., & Coleman, J. N. (2016). Production of Highly Monolayer Enriched Dispersions of Liquid-Exfoliated Nanosheets by Liquid Cascade Centrifugation. *ACS Nano*, *10*(1), 1589–1601. <https://doi.org/10.1021/acsnano.5b07228>

- Baker, J., Watson, T. M., Jones, D., Deganello, D., Gethin, D. T., & Claypole, T. C. (2014). Optically transparent graphene nanoplatelet inks as low cost electrocatalysts for liquid dye sensitised solar cells. *MRS Proceedings*, 1667, mrss14-1667-b12-04. <https://doi.org/10.1557/opl.2014.684>
- Barmpakos, D., Belessi, V., Schelwald, R., & Kaltsas, G. (2021). *Evaluation of Inkjet-Printed Reduced and Functionalized Water-Dispersible Graphene Oxide and Graphene on Polymer Substrate — Application to Printed Temperature Sensors*.
- Barmpakos, D., & Kaltsas, G. (2021). A review on humidity, temperature and strain printed sensors—current trends and future perspectives. *Sensors (Switzerland)*, 21(3), 1–24. <https://doi.org/10.3390/s21030739>
- Barton, A. F. M. (1983). *CRC Handbook of Solubility Parameters*.
- BFPA. (2017). *British Fluid Power Association*. BFPA Chairs and Delivers the Opening Address at the 2017 Appetite for Engineering Conference. <https://bfpa.co.uk/newsletter/bfpa-chairs-delivers-opening-address-2017-appetite-engineering-conference/>
- Bhuyan, M. S. A., Uddin, M. N., Islam, M. M., Bipasha, F. A., & Hossain, S. S. (2016). Synthesis of graphene. *International Nano Letters*, 6(2), 65–83. <https://doi.org/10.1007/s40089-015-0176-1>
- Bianchi, V., Carey, T., Viti, L., Li, L., Linfield, E. H., Davies, A. G., Tredicucci, A., Yoon, D., Karagiannidis, P. G., Lombardi, L., Tomarchio, F., Ferrari, A. C., Torrisi, F., & Vitiello, M. S. (2017). Terahertz saturable absorbers from liquid phase exfoliation of graphite. *Nature Communications*, 8, 1–9. <https://doi.org/10.1038/ncomms15763>
- Brennan, B., Spencer, S. J., Belsey, N. A., Faris, T., Cronin, H., Silva, S. R. P., Sainsbury, T., Gilmore, I. S., Stoeva, Z., & Pollard, A. J. (2017). Structural, chemical and electrical characterisation of conductive graphene-polymer composite films. *Applied Surface Science*, 403, 403–412. <https://doi.org/10.1016/j.apsusc.2017.01.132>
- Burman, D., Santra, S., Pramanik, P., & Guha, P. K. (2018). Pt decorated MoS₂ nanoflakes for ultrasensitive resistive humidity sensor. *Nanotechnology*, 29(11), 115504. <https://doi.org/10.1088/1361-6528/aaa79d>
- Byrne, F. P., Jin, S., Paggiola, G., Petchey, T. H. M., Clark, J. H., Farmer, T. J., Hunt, A. J., Robert McElroy, C., & Sherwood, J. (2016). Tools and techniques for solvent selection: green solvent selection guides. *Sustainable Chemical Processes*, 4(1), 7. <https://doi.org/10.1186/s40508-016-0051-z>

- Capasso, A., Del Rio Castillo, A. E., Sun, H., Ansaldo, A., Pellegrini, V., & Bonaccorso, F. (2015). Ink-jet printing of graphene for flexible electronics: An environmentally-friendly approach. *Solid State Communications*, 224, 53–63. <https://doi.org/10.1016/j.ssc.2015.08.011>
- Carey, T., Cacovich, S., Divitini, G., Ren, J., Mansouri, A., Kim, J. M., Wang, C., Ducati, C., Sordan, R., & Torrisi, F. (2017). Fully inkjet-printed two-dimensional material field-effect heterojunctions for wearable and textile electronics. *Nature Communications*, 8(1). <https://doi.org/10.1038/s41467-017-01210-2>
- Carl L. Yaws. (2008). *Thermophysical Properties of Chemicals and Hydrocarbons 1st Edition*.
- Chen, C., Wang, X., Li, M., Fan, Y., & Sun, R. (2018). Humidity sensor based on reduced graphene oxide/lignosulfonate composite thin-film. *Sensors and Actuators, B: Chemical*, 255, 1569–1576. <https://doi.org/10.1016/j.snb.2017.08.168>
- Chen, G., Qiao, C., Wang, Y., & Yao, J. (2014). Synthesis of biocompatible gelatin-functionalised graphene nanosheets for drug delivery applications. *Australian Journal of Chemistry*, 67(10), 1532–1537. <https://doi.org/10.1071/CH13678>
- Chen, H., Zhang, Y., Ma, Y., Chen, S., Wu, Y., Lu, Y., Ren, H., Xin, S., & Bai, Y. (2021). Sand-Milling Exfoliation of Structure Controllable Graphene for Formulation of Highly Conductive and Multifunctional Graphene Inks. *Advanced Materials Interfaces*, 8(1), 1–10. <https://doi.org/10.1002/admi.202000888>
- Chen, Z., & Lu, C. (2005). Humidity sensors: A review of materials and mechanisms. *Sensor Letters*, 3(4), 274–295. <https://doi.org/10.1166/sl.2005.045>
- Chernozatonskii, L. A., Sorokin, P. B., Belova, E. É., Brüning, J., & Fedorov, A. S. (2006). Metal-semiconductor (semimetal) superlattices on a graphite sheet with vacancies. *JETP Letters*, 84(3), 115–118. <https://doi.org/10.1134/S0021364006150033>
- Choi, K. H., Sajid, M., Aziz, S., & Yang, B.-S. (2015). Wide range high speed relative humidity sensor based on PEDOT:PSS–PVA composite on an IDT printed on piezoelectric substrate. *Sensors and Actuators A: Physical*, 228, 40–49. <https://doi.org/10.1016/j.sna.2015.03.003>
- Coats, A. W., & Redfern, J. P. (1963). Thermogravimetric analysis. A review. *The Analyst*, 88(1053), 906. <https://doi.org/10.1039/an9638800906>
- Decaens, J., & Vermeersch, O. (2016). Wearable technologies for personal protective equipment: Embedded textile monitoring sensors, power and data transmission, end-life indicators. In *Smart Textiles and Their Applications*. Elsevier Ltd. <https://doi.org/10.1016/B978-0-08-100574-3.00023-0>

- Dincer, C., Bruch, R., Costa-Rama, E., Fernández-Abedul, M. T., Merkoçi, A., Manz, A., Urban, G. A., & Güder, F. (2019). Disposable Sensors in Diagnostics, Food, and Environmental Monitoring. *Advanced Materials*, *31*(30).
<https://doi.org/10.1002/adma.201806739>
- Dodoo-Arhin, D., Howe, R. C. T., Hu, G., Zhang, Y., Hiralal, P., Bello, A., Amaratunga, G., & Hasan, T. (2016). Inkjet-printed graphene electrodes for dye-sensitized solar cells. *Carbon*, *105*(April), 33–41. <https://doi.org/10.1016/j.carbon.2016.04.012>
- Dogara, M. D., Isaac, H. D., Gyuk, P. M., & Iyen, C. (2018). Comparison Between a Constructed Arduino Based System and Keithley Sourcemeter 2400 on Some Electronics Devices. *Science World Journal*, *13*(2), 55–57.
- Dyson, D. M. (2021). *Printed Electronic News* (p. 3). IDTechEx.
www.IDTechEx.com/flexsensors
- Ertu, B. (2012). The Fabrication of Porous Barium Titanate Ceramics via Pore-Forming Agents (PFAs) for Thermistor and Sensor Applications. *Powder Metallurgy*, September.
<https://doi.org/10.5772/33930>
- Expanding the Vision of Sensor Materials. (1995). In *Expanding the Vision of Sensor Materials*. <https://doi.org/10.17226/4782>
- Farahani, H., Wagiran, R., & Hamidon, M. N. (2014). Humidity sensors principle, mechanism, and fabrication technologies: A comprehensive review. In *Sensors (Switzerland)* (Vol. 14, Issue 5). <https://doi.org/10.3390/s140507881>
- Filly, A., Fabiano-Tixier, A. S., Louis, C., Fernandez, X., & Chemat, F. (2016). Water as a green solvent combined with different techniques for extraction of essential oil from lavender flowers. *Comptes Rendus Chimie*, *19*(6), 707–717.
<https://doi.org/10.1016/j.crci.2016.01.018>
- Gligoric, N., Krco, S., Hakola, L., Vehmas, K., De, S., Moessner, K., Jansson, K., Polenz, I., & Van Kranenburg, R. (2019). Smarttags: IoT product passport for circular economy based on printed sensors and unique item-level identifiers. *Sensors (Switzerland)*, *19*(3).
<https://doi.org/10.3390/s19030586>
- Hajian, S., Zhang, X., Khakbaz, P., Tabatabaei, S. M., Maddipatla, D., Narakathu, B. B., Blair, R. G., & Atashbar, M. Z. (2020). Development of a Fluorinated Graphene-Based Resistive Humidity Sensor. *IEEE Sensors Journal*, *20*(14), 7517–7524.
<https://doi.org/10.1109/JSEN.2020.2985055>
- Hartonen, K., & Riekkola, M.-L. (2017). Water as the First Choice Green Solvent. In *The Application of Green Solvents in Separation Processes* (pp. 19–55). Elsevier.
<https://doi.org/10.1016/B978-0-12-805297-6.00002-4>

- Helmut Kipphan. (2001). *Handbook of print media technologies and production methods*. Springer.
- Henry Pohs. (1995). *The Miner's Flame Light Book*. Flame Publishing Company.
- Hernandez, Y., Lotya, M., Rickard, D., Bergin, S. D., & Coleman, J. N. (2010). Measurement of Multicomponent Solubility Parameters for Graphene Facilitates Solvent Discovery. *Langmuir*, 26(5), 3208–3213. <https://doi.org/10.1021/la903188a>
- Hossain, R. F., Deaguero, I. G., Boland, T., & Kaul, A. B. (2017). Biocompatible, large-format, inkjet printed heterostructure MoS₂-graphene photodetectors on conformable substrates. *Npj 2D Materials and Applications*, 1(1), 1–9. <https://doi.org/10.1038/s41699-017-0034-2>
- Htwe, Y. Z. N., Abdullah, M. K., & Mariatti, M. (2021). Optimization of graphene conductive ink using solvent exchange techniques for flexible electronics applications. *Synthetic Metals*, 274(January), 116719. <https://doi.org/10.1016/j.synthmet.2021.116719>
- Htwe, Y. Z. N., & Mariatti, M. (2021). Surfactant-assisted water-based graphene conductive inks for flexible electronic applications. *Journal of the Taiwan Institute of Chemical Engineers*, 125, 402–412. <https://doi.org/10.1016/j.jtice.2021.06.022>
- Hu, G., Kang, J., Ng, L. W. T., Zhu, X., Howe, R. C. T., Jones, C. G., Hersam, M. C., & Hasan, T. (2018). Functional inks and printing of two-dimensional materials. *Chemical Society Reviews*, 47(9), 3265–3300. <https://doi.org/10.1039/c8cs00084k>
- Hyun, W. J., Secor, E. B., Hersam, M. C., Frisbie, C. D., & Francis, L. F. (2015). High-resolution patterning of graphene by screen printing with a silicon stencil for highly flexible printed electronics. *Advanced Materials*, 27(1), 109–115. <https://doi.org/10.1002/adma.201404133>
- James, F. A. J. L. (1994). David Knight, Humphry Davy: Science and Power. Oxford: Blackwell, 1992. Pp. xiii + 218. ISBN 0-631-16816-8. £30.00. *The British Journal for the History of Science*, 27(2), 230–231. <https://doi.org/10.1017/S0007087400032015>
- Jarosz, A., Skoda, M., Dudek, I., & Szukiewicz, D. (2016). Oxidative Stress and Mitochondrial Activation as the Main Mechanisms Underlying Graphene Toxicity against Human Cancer Cells. *Oxidative Medicine and Cellular Longevity*, 2016. <https://doi.org/10.1155/2016/5851035>
- Jeong, H., Noh, Y., & Lee, D. (2019). Highly stable and sensitive resistive flexible humidity sensors by means of roll-to-roll printed electrodes and flower-like TiO₂ nanostructures. *Ceramics International*, 45(1), 985–992. <https://doi.org/10.1016/j.ceramint.2018.09.276>

- Jeong, Y., Hong, S., Jung, G., Shin, W., Park, J., Kim, D., Choi, Y. S., Bae, J. H., Hong, B. H., & Lee, J. H. (2021). Highly stable Si MOSFET-type humidity sensor with ink-jet printed graphene quantum dots sensing layer. *Sensors and Actuators, B: Chemical*, *343*(May), 130134. <https://doi.org/10.1016/j.snb.2021.130134>
- Johnson, D. W., Dobson, B. P., & Coleman, K. S. (2015). A manufacturing perspective on graphene dispersions. *Current Opinion in Colloid and Interface Science*, *20*(5–6), 367–382. <https://doi.org/10.1016/j.cocis.2015.11.004>
- Johnson, M. (2013). Detergents: Triton X-100, Tween-20, and More. *Materials and Methods*, *3*. <https://doi.org/10.13070/mm.en.3.163>
- Juntunen, T., Jussila, H., Ruoho, M., Liu, S., Hu, G., Albrow-Owen, T., Ng, L. W. T., Howe, R. C. T., Hasan, T., Sun, Z., & Tittonen, I. (2018). Inkjet Printed Large-Area Flexible Few-Layer Graphene Thermoelectrics. *Advanced Functional Materials*, *28*(22). <https://doi.org/10.1002/adfm.201800480>
- Kamarudin, S. F., Mustapha, M., & Kim, J. K. (2021). Green Strategies to Printed Sensors for Healthcare Applications. *Polymer Reviews*, *61*(1), 116–156. <https://doi.org/10.1080/15583724.2020.1729180>
- Karagiannidis, P. G., Hodge, S. A., Lombardi, L., Tomarchio, F., Decorde, N., Milana, S., Goykhman, I., Su, Y., Mesite, S. V., Johnstone, D. N., Leary, R. K., Midgley, P. A., Pugno, N. M., Torrisi, F., & Ferrari, A. C. (2017). Microfluidization of Graphite and Formulation of Graphene-Based Conductive Inks. *ACS Nano*, *11*(3), 2742–2755. <https://doi.org/10.1021/acsnano.6b07735>
- Khalifa, M., Wuzella, G., Lammer, H., & Mahendran, A. R. (2020). Smart paper from graphene coated cellulose for high-performance humidity and piezoresistive force sensor. *Synthetic Metals*, *266*(May), 116420. <https://doi.org/10.1016/j.synthmet.2020.116420>
- Khan, M. U., Hassan, G., Awais, M., & Bae, J. (2020). All printed full range humidity sensor based on Fe₂O₃. *Sensors and Actuators A: Physical*, *311*, 112072. <https://doi.org/10.1016/j.sna.2020.112072>
- Kim, D.-U., & Gong, M.-S. (2005). Thick films of copper-titanate resistive humidity sensor. *Sensors and Actuators B: Chemical*, *110*(2), 321–326. <https://doi.org/10.1016/j.snb.2005.02.010>
- Kim, D. S., Jeong, J. M., Park, H. J., Kim, Y. K., Lee, K. G., & Choi, B. G. (2021). Highly Concentrated, Conductive, Defect-free Graphene Ink for Screen-Printed Sensor Application. *Nano-Micro Letters*, *13*(1). <https://doi.org/10.1007/s40820-021-00617-3>

- Kim, M.-J., & Gong, M.-S. (2012). Water-resistive humidity sensor prepared by printing process using polyelectrolyte ink derived from new monomer. *The Analyst*, 137(6), 1487. <https://doi.org/10.1039/c2an15800k>
- Kipphan, H. (2001). Handbook of Print Media. In *Print and Paper Europe* (Vol. 13, Issue 6). <https://doi.org/10.1007/978-3-540-29900-4>
- Kuang, Q., Lao, C., Zhong, L. W., Xie, Z., & Zheng, L. (2007). High-sensitivity humidity sensor based on a single SnO₂ nanowire. *Journal of the American Chemical Society*, 129(19), 6070–6071. <https://doi.org/10.1021/ja070788m>
- Kulkarni, M. V., Apte, S. K., Naik, S. D., Ambekar, J. D., & Kale, B. B. (2012). P1.8.3 Ink-Jet Printed Conducting Polyaniline based Flexible Humidity Sensor. *Proceedings IMCS 2012*, 1112–1115. <https://doi.org/10.5162/IMCS2012/P1.8.3>
- Kulwicki, B. M. (1991). Humidity Sensors. *Journal of the American Ceramic Society*, 74(4), 697–708. <https://doi.org/10.1111/j.1151-2916.1991.tb06911.x>
- Kutzner, C., Lucklum, R., Torah, R., Beeby, S., & Tudor, J. (2013). Novel screen printed humidity sensor on textiles for smart textile applications. *2013 Transducers & Eurosensors XXVII: The 17th International Conference on Solid-State Sensors, Actuators and Microsystems (TRANSDUCERS & EUROSENSORS XXVII)*, 282–285. <https://doi.org/10.1109/Transducers.2013.6626757>
- Landi, G, Sorrentino, A., Iannace, S., & Neitzert, H. C. (2017). Differences between graphene and graphene oxide in gelatin based systems for transient biodegradable energy storage applications. *Nanotechnology*, 28(5), 054005. <https://doi.org/10.1088/1361-6528/28/5/054005>
- Landi, Giovanni, Fedi, F., Sorrentino, A., Neitzert, H. C., & Iannace, S. (2014). *Gelatin/graphene systems for low cost energy storage*. 202–205. <https://doi.org/10.1063/1.4876813>
- Landi, Giovanni, Neitzert, H. C., & Sorrentino, A. (2018). *New biodegradable nanocomposites for transient electronics devices*. 020012. <https://doi.org/10.1063/1.5047766>
- Landi, Giovanni, Sorrentino, A., Fedi, F., Neitzert, H. C., & Iannace, S. (2015). Cycle stability and dielectric properties of a new biodegradable energy storage material. *Nano Energy*, 17, 348–355. <https://doi.org/10.1016/j.nanoen.2015.09.006>
- Landi, Giovanni, Sorrentino, A., Iannace, S., & Neitzert, H. C. (2015). Electrical Characterization and Modeling of a Gelatin/Graphene System. *Advances in Condensed Matter Physics*, 2015, 1–5. <https://doi.org/10.1155/2015/107957>

- Lau, A. K. T., & Hui, D. (2002). The revolutionary creation of new advanced materials - Carbon nanotube composites. *Composites Part B:Engineering*, 33(4), 263–277. [https://doi.org/10.1016/S1359-8368\(02\)00012-4](https://doi.org/10.1016/S1359-8368(02)00012-4)
- Lee, C. Y., & Lee, G. Bin. (2005). Humidity sensors: A review. *Sensor Letters*, 3(1), 1–15. <https://doi.org/10.1166/sl.2005.001>
- Li, J., Ye, F., Vaziri, S., Muhammed, M., Lemme, M. C., & Östling, M. (2013). Efficient inkjet printing of graphene. *Advanced Materials*, 25(29), 3985–3992. <https://doi.org/10.1002/adma.201300361>
- Liang, B., Liu, K., Liu, P., Qian, L., Zhao, G., Pan, W., & Chen, C. (2021). Organic salt-assisted liquid-phase shear exfoliation of expanded graphite into graphene nanosheets. *Journal of Materiomics*, xxxx, 1–9. <https://doi.org/10.1016/j.jmat.2021.03.007>
- Liang, Y. T., & Hersam, M. C. (2010). Highly Concentrated Graphene Solutions via Polymer Enhanced Solvent Exfoliation and Iterative Solvent Exchange. *Journal of the American Chemical Society*, 132(50), 17661–17663. <https://doi.org/10.1021/ja107661g>
- Lim, D.-I., Cha, J.-R., & Gong, M.-S. (2013). Preparation of flexible resistive micro-humidity sensors and their humidity-sensing properties. *Sensors and Actuators B: Chemical*, 183, 574–582. <https://doi.org/10.1016/j.snb.2013.04.031>
- Lv, C., Hu, C., Luo, J., Liu, S., Qiao, Y., Zhang, Z., Song, J., Shi, Y., Cai, J., & Watanabe, A. (2019). Recent Advances in Graphene-Based Humidity Sensors. *Nanomaterials*, 9(3), 422. <https://doi.org/10.3390/nano9030422>
- Ma, Y., & Zhi, L. (2019). Graphene-Based Transparent Conductive Films: Material Systems, Preparation and Applications. *Small Methods*, 3(1), 1–32. <https://doi.org/10.1002/smtd.201800199>
- MAJEWSKI, J. (2016). Polymer-based sensors for measurement of low humidity in air and industrial gases. *Przeegląd Elektrotechniczny*, 1(8), 76–79. <https://doi.org/10.15199/48.2016.08.20>
- Martínez-Flores, R., Canto-Aguilar, E. J., Rodríguez-Gattorno, G., Oskam, G., Meneses-Rodríguez, D., & Ruiz-Gómez, M. A. (2019). Inkjet-Printed Reduced Graphene Oxide (rGO) Films For Electrocatalytic Applications. *Journal of The Electrochemical Society*, 166(5), H3279–H3285. <https://doi.org/10.1149/2.0381905jes>
- McManus, D., Vranic, S., Withers, F., Sanchez-Romaguera, V., Macucci, M., Yang, H., Sorrentino, R., Parvez, K., Son, S.-K., Iannaccone, G., Kostarelos, K., Fiori, G., & Casiraghi, C. (2017). Water-based and biocompatible 2D crystal inks for all-inkjet-printed heterostructures. *Nature Nanotechnology*, 12(4), 343–350. <https://doi.org/10.1038/nnano.2016.281>

- Montgomery, R., & McDowall, R. (2008). Sensors and Auxiliary Devices. *Fundamentals of HVAC Control Systems*, 106–159. <https://doi.org/10.1016/b978-0-08-055233-0.00004-2>
- Mujumdar, A. S. (1987). Moisture Sensors in Process Control. *Drying Technology*, 5(3), 485–486. <https://doi.org/10.1080/07373938708916556>
- Nayak, L., Mohanty, S., & Ramadoss, A. (2021). A green approach to water-based graphene ink with reverse coffee ring effect. *Journal of Materials Science: Materials in Electronics*, 32(6), 7431–7442. <https://doi.org/10.1007/s10854-021-05456-x>
- Nežerka, V., Somr, M., & Trejbal, J. (2018). Contact Angle Measurement Tool Based on Image Analysis. *Experimental Techniques*, 42(3), 271–278. <https://doi.org/10.1007/s40799-017-0231-0>
- Phuyal, S., Bista, D., & Bista, R. (2020). Challenges, Opportunities and Future Directions of Smart Manufacturing: A State of Art Review. *Sustainable Futures*, 2, 100023. <https://doi.org/10.1016/j.sftr.2020.100023>
- Rittersma, Z. M. (2002). Recent achievements in miniaturised humidity sensors - A review of transduction techniques. *Sensors and Actuators, A: Physical*, 96(2–3), 196–210. [https://doi.org/10.1016/S0924-4247\(01\)00788-9](https://doi.org/10.1016/S0924-4247(01)00788-9)
- Salavagione, H. J., Shuttleworth, P. S., Fernández-Blázquez, J. P., Ellis, G. J., & Gómez-Fatou, M. A. (2020). Scalable graphene-based nanocomposite coatings for flexible and washable conductive textiles. *Carbon*, 167, 495–503. <https://doi.org/10.1016/j.carbon.2020.05.108>
- Santra, S., Hu, G., Howe, R. C. T., De Luca, A., Ali, S. Z., Udrea, F., Gardner, J. W., Ray, S. K., Guha, P. K., & Hasan, T. (2015). CMOS integration of inkjet-printed graphene for humidity sensing. *Scientific Reports*, 5, 1–12. <https://doi.org/10.1038/srep17374>
- Sarvari, R., Sattari, S., Massoumi, B., Agbolaghi, S., Beygi-Khosrowshahi, Y., & Kahaie-Khosrowshahi, A. (2017). Composite electrospun nanofibers of reduced graphene oxide grafted with poly(3-dodecylthiophene) and poly(3-thiophene ethanol) and blended with polycaprolactone. *Journal of Biomaterials Science, Polymer Edition*, 28(15), 1740–1761. <https://doi.org/10.1080/09205063.2017.1354167>
- Satapathy, M. K., Chiang, W.-H., Chuang, E.-Y., Chen, C.-H., Liao, J.-L., & Huang, H.-N. (2017). Microplasma-assisted hydrogel fabrication: A novel method for gelatin-graphene oxide nano composite hydrogel synthesis for biomedical application. *PeerJ*, 5, e3498. <https://doi.org/10.7717/peerj.3498>
- Schedin, F., Geim, A. K., Morozov, S. V., Hill, E. W., Blake, P., Katsnelson, M. I., & Novoselov, K. S. (2007). Detection of individual gas molecules adsorbed on graphene. *Nature Materials*, 6(9), 652–655. <https://doi.org/10.1038/nmat1967>

- Secor, E. B. (2018). Principles of aerosol jet printing. *Flexible and Printed Electronics*, 3(3), 1–31. <https://doi.org/10.1088/2058-8585/aace28>
- Secor, E. B., Gao, T. Z., Islam, A. E., Rao, R., Wallace, S. G., Zhu, J., Putz, K. W., Maruyama, B., & Hersam, M. C. (2017). Enhanced Conductivity, Adhesion, and Environmental Stability of Printed Graphene Inks with Nitrocellulose. *Chemistry of Materials*, 29(5), 2332–2340. <https://doi.org/10.1021/acs.chemmater.7b00029>
- Secor, E. B., Lim, S., Zhang, H., Frisbie, C. D., Francis, L. F., & Hersam, M. C. (2014). Gravure printing of graphene for large-area flexible electronics. *Advanced Materials*, 26(26), 4533–4538. <https://doi.org/10.1002/adma.201401052>
- Shin, K.-Y., Hong, J.-Y., & Jang, J. (2011). Micropatterning of Graphene Sheets by Inkjet Printing and Its Wideband Dipole-Antenna Application. *Advanced Materials*, 23(18), 2113–2118. <https://doi.org/10.1002/adma.201100345>
- Shojaee, M., Nasresfahani, S., Dordane, M. K., & Sheikhi, M. H. (2018). Fully integrated wearable humidity sensor based on hydrothermally synthesized partially reduced graphene oxide. *Sensors and Actuators A: Physical*, 279, 448–456. <https://doi.org/10.1016/j.sna.2018.06.052>
- Sikarwar, S., & Yadav, B. C. (2015). Opto-electronic humidity sensor: A review. *Sensors and Actuators, A: Physical*, 233(May), 54–70. <https://doi.org/10.1016/j.sna.2015.05.007>
- Sinha Ray, S. (2013). Techniques for characterizing the structure and properties of polymer nanocomposites. In *Environmentally Friendly Polymer Nanocomposites* (pp. 74–88). Elsevier. <https://doi.org/10.1533/9780857097828.1.74>
- Sriprachubwong, C., Karuwan, C., Wisitsorrat, A., Phokharatkul, D., Lomas, T., Sritongkham, P., & Tuantranont, A. (2012). Inkjet-printed graphene-PEDOT:PSS modified screen printed carbon electrode for biochemical sensing. *Journal of Materials Chemistry*, 22(12), 5478–5485. <https://doi.org/10.1039/c2jm14005e>
- Stefan, R. I., Van Staden, J. F., & Aboul-Enein, H. Y. (2004). Biosensor technology. In *Analytical Instrumentation Handbook, Third Edition*. <https://doi.org/10.1201/9781315118024-21>
- Suganuma, K. (2014). *Introduction to printed electronics (SpringerBriefs in electrical and computer engineering)*.
- Sun, A., Huang, L., & Li, Y. (2009). Study on humidity sensing property based on TiO₂ porous film and polystyrene sulfonic sodium. *Sensors and Actuators, B: Chemical*, 139(2), 543–547. <https://doi.org/10.1016/j.snb.2009.03.064>

- The Chemical Rubber Company. (1969). *CRC Handbook of Chemistry and Physics, 50th Edition* (R. C. Weast (ed.); 50th ed.).
- Tkachev, S., Monteiro, M., Santos, J., Placidi, E., Hassine, M. Ben, Marques, P., Ferreira, P., Alpuim, P., & Capasso, A. (2021). Environmentally Friendly Graphene Inks for Touch Screen Sensors. *Advanced Functional Materials*, 2103287, 1–15. <https://doi.org/10.1002/adfm.202103287>
- Torrise, F., Hasan, T., Wu, W., Sun, Z., Lombardo, A., Kulmala, T. S., Hsieh, G.-W., Jung, S., Bonaccorso, F., Paul, P. J., Chu, D., & Ferrari, A. C. (2012). Inkjet-Printed Graphene Electronics. *ACS Nano*, 6(4), 2992–3006. <https://doi.org/10.1021/nn2044609>
- Tung, T. T., Nine, M. J., Krebsz, M., Pasinszki, T., Coghlan, C. J., Tran, D. N. H., & Losic, D. (2017). Recent Advances in Sensing Applications of Graphene Assemblies and Their Composites. *Advanced Functional Materials*, 27(46). <https://doi.org/10.1002/adfm.201702891>
- Turkani, V. S., Narakathu, B. B., Maddipatla, D., Bazuin, B. J., & Atashbar, M. Z. (2018). P1FW.5 - A Fully Printed CNT Based Humidity Sensor on Flexible PET Substrate. *Proceedings IMCS 2018*, 519–520. <https://doi.org/10.5162/IMCS2018/P1FW.5>
- Turkani, Vikram S., Maddipatla, D., Narakathu, B. B., Saeed, T. S., Obare, S. O., Bazuin, B. J., & Atashbar, M. Z. (2019). A highly sensitive printed humidity sensor based on a functionalized MWCNT/HEC composite for flexible electronics application. *Nanoscale Advances*, 1(6), 2311–2322. <https://doi.org/10.1039/C9NA00179D>
- Vuorinen, T., Niittynen, J., Kankkunen, T., Kraft, T. M., & Mäntysalo, M. (2016). Inkjet-printed graphene/PEDOT:PSS temperature sensors on a skin-conformable polyurethane substrate. *Scientific Reports*, 6(September), 1–8. <https://doi.org/10.1038/srep35289>
- Wang, S., Zhang, Y., Abidi, N., & Cabrales, L. (2009). Wettability and Surface Free Energy of Graphene Films. *Langmuir*, 25(18), 11078–11081. <https://doi.org/10.1021/la901402f>
- Wassei, J. K., & Kaner, R. B. (2010). Graphene, a promising transparent conductor. *Materials Today*, 13(3), 52–59. [https://doi.org/10.1016/S1369-7021\(10\)70034-1](https://doi.org/10.1016/S1369-7021(10)70034-1)
- Xu, C.-Y., Shi, X.-M., Guo, L., Wang, X., Wang, X.-Y., & Li, J.-Y. (2017). Optimization of Graphene Conductive Ink with 73 wt% Graphene Contents. *Journal of Nanoscience and Nanotechnology*, 18(6), 4014–4021. <https://doi.org/10.1166/jnn.2018.15201>
- Xu, Y., Hennig, I., Freyberg, D., James Strudwick, A., Georg Schwab, M., Weitz, T., & Chih-Pei Cha, K. (2014). Inkjet-printed energy storage device using graphene/polyaniline inks. *Journal of Power Sources*, 248, 483–488. <https://doi.org/10.1016/j.jpowsour.2013.09.096>

- Xu, Y., Schwab, M. G., Strudwick, A. J., Hennig, I., Feng, X., Wu, Z., & Müllen, K. (2013). Screen-printable thin film supercapacitor device utilizing graphene/polyaniline inks. *Advanced Energy Materials*, 3(8), 1035–1040. <https://doi.org/10.1002/aenm.201300184>
- Yadav, A. (2018). Classification and Applications of Humidity Sensors: A Review. *International Journal for Research in Applied Science and Engineering Technology*, 6(4), 3686–3699. <https://doi.org/10.22214/ijraset.2018.4616>
- Yamazoe, N., & Shimizu, Y. (1986). Humidity sensors: Principles and applications. *Sensors and Actuators*, 10(3–4), 379–398. [https://doi.org/10.1016/0250-6874\(86\)80055-5](https://doi.org/10.1016/0250-6874(86)80055-5)
- Yu, D., Li, J., Wang, T., She, X., Sun, Y., Li, J., Zhang, L., Yu, X. F., & Yang, D. (2020). Black Phosphorus All-Fiber Sensor for Highly Responsive Humidity Detection. *Physica Status Solidi - Rapid Research Letters*, 14(4), 1–6. <https://doi.org/10.1002/pssr.201900697>
- Zhang, D., Chang, H., & Liu, R. (2016). Humidity-Sensing Properties of One-Step Hydrothermally Synthesized Tin Dioxide-Decorated Graphene Nanocomposite on Polyimide Substrate. *Journal of Electronic Materials*, 45(8), 4275–4281. <https://doi.org/10.1007/s11664-016-4630-2>
- Zhang, R., Peng, B., & Yuan, Y. (2018). Flexible printed humidity sensor based on poly(3,4-ethylenedioxythiophene)/reduced graphene oxide/Au nanoparticles with high performance. *Composites Science and Technology*, 168, 118–125. <https://doi.org/10.1016/j.compscitech.2018.09.013>
- Zhang, X., Turkani, V. S., Hajian, S., Bose, A. K., Maddipatla, D., Hanson, A. J., Narakathu, B. B., & Atashbar, M. Z. (2019). Novel Printed Carbon Nanotubes Based Resistive Humidity Sensors. *2019 IEEE International Conference on Flexible and Printable Sensors and Systems (FLEPS)*, 1–3. <https://doi.org/10.1109/FLEPS.2019.8792298>
- Zhang, Xingzhe, Maddipatla, D., Bose, A. K., Hajian, S., Narakathu, B. B., Williams, J. D., Mitchell, M. F., & Atashbar, M. Z. (2020). Printed Carbon Nanotubes-Based Flexible Resistive Humidity Sensor. *IEEE Sensors Journal*, 20(21), 12592–12601. <https://doi.org/10.1109/JSEN.2020.3002951>
- Zhao, J., Li, N., Yu, H., Wei, Z., Liao, M., Chen, P., Wang, S., Shi, D., Sun, Q., & Zhang, G. (2017). Highly Sensitive MoS₂ Humidity Sensors Array for Noncontact Sensation. *Advanced Materials*, 29(34), 1–7. <https://doi.org/10.1002/adma.201702076>